MID-AMERICA TRANSPORTATION CENTER

Report # MATC-MS&T: 131-1

Final Report
WBS: 25-1121-0005-131-1

Sensor-Assisted Condition Evaluation of Steel and Prestressed Concrete Girder Bridges Subjected to Fire - Phase I

Genda Chen, PhD, PE
Professor and Robert W Abbett Distinguished Chair in Civil Engineering
Department of Civil, Architectural, and Environmental Engineering
Missouri University of Science and Technology

Yanping Zhu
PhD Candidate

Yi Bao, PhD
Assistant Professor
Department of Civil, Environmental, and Ocean Engineering
Stevens Institute of Technology

2020

A Cooperative Research Project sponsored by
U.S. Department of Transportation- Office of the Assistant Secretary for Research and Technology

Sensor-Assisted Condition Evaluation of Steel and Prestressed Concrete Girder Bridges – Phase I

Genda Chen, Ph.D., P.E., F. ASCE
Professor and Robert W. Abbett Distinguished Chair in Civil Engineering
Director, Center for Intelligent Infrastructure
Director, INSPIRE University Transportation Center
Associate Director, Mid-America Transportation Center
Department of Civil, Architectural, and Environmental Engineering
Missouri University of Science and Technology

Yanping Zhu, Ph.D. Candidate
Department of Civil, Architectural, and Environmental Engineering
Missouri University of Science and Technology

Yi Bao, Ph.D. Assistant Professor
Department of Civil, Environmental and Ocean Engineering
Stevens Institute of Technology

A Report on Research Sponsored by

Mid-America Transportation Center

University of Nebraska–Lincoln

December 2020

Technical Report Documentation Page

1. Report No. 25-1121-0005-131-1	2. Government Accession No.	3. Recipient's Catalog No.
4. Title and Subtitle Sensor-Assisted Condition Evaluation of Steel and Prestressed Concrete Girder Bridges Subjected to Fire – Phase I		5. Report Date December 2020
		6. Performing Organization Code
7. Author(s) Yanping Zhu, Genda Chen, and Yi Bao		8. Performing Organization Report No. 25-1121-0005-131-1
9. Performing Organization Name and Address Center for Intelligent Infrastructure Department of Civil, Architectural, and Environmental Engineering Missouri University of Science and Technology 500 W. 16th Street Rolla, MO 65409-0810		10. Work Unit No. (TRAIS)
		11. Contract or Grant No. 69A3551747107
12. Sponsoring Agency Name and Address Mid-America Transportation Center 2200 Vine St PO Box 830851 Lincoln, NE 68583-0851		13. Type of Report and Period Covered Final Report August 1, 2017 - December 31, 2020
		14. Sponsoring Agency Code MATC TRB RiP No. 91994-17
15. Supplementary Notes		

16. Abstract

This report summarizes the results and findings of Mid-America Transportation Research Center (MATC) research project No. 59709. It is focused on the measurement of strain and temperature in concrete structures during or after exposure to high temperatures using pulse pre-pump Brillouin optical time domain analysis (PPP-BOTDA). The main objectives of this study are: (a) to study the strain transfer in concrete after exposure to high temperatures using PPP-BOTDA based fiber optic sensors; (b) to apply distributed fiber optic sensing (DFOS) technology based on PPP-BOTDA in large-scale concrete slabs. Dog-bone shaped ultra-high performance mortar was fabricated with DFOS embedded. They were subjected to different high temperatures and then natural cooling. After that, they were tested under tension. PPP-BOTDA based strain results compared well with the strain gauge data. This test demonstrates the effectiveness of strain transfer between the fiber optic sensors and concrete after exposure to high temperatures due to the occurrence of melting residues which provide friction between them. Several large-scale composite floor beams were fabricated and tested under mechanical or combined mechanical and fire conditions. The concrete slabs were instrumented with DFOS technology in an attempt to measure temperature distribution. Comparisons with co-located thermocouples show that while the increased spatial resolution provides new insights about temperature phenomena, challenges for local temperature measurements were encountered during this first attempt at application to large-scale specimens.

17. ORCID No. of each Researcher Genda Chen: 0000-0002-0658-4356	18. Distribution Statement		
19. Security Classif. (of this report) Unclassified	20. Security Classif. (of this page) Unclassified	21. No. of Pages 67	22. Price

Table of Contents

List of Figures

List of Tables

Acknowledgments

Financial support was provided by Mid-America Transportation Research Center under contract agreement No. 59709. Thanks are due to Drs. Chuanrui Guo, Liang Fan, and Mr. Xinzhe Yuan, for their assistance during early tests of the beams. The large-scale composite floor beams were cast and tested by research staff in the National Fire Laboratory at National Institute of Standards and Technology under the leadership of Lisa Choe and Matthew S. Hoehler.

Disclaimer

The contents of this report reflect the views of the authors, who are responsible for the facts and the accuracy of the information presented herein. This document is disseminated in the interest of information exchange. The report is funded, partially or entirely, by a grant from the U.S. Department of Transportation's University Transportation Centers Program. However, the U.S. Government assumes no liability for the contents or use thereof.

Abstract

This report summarizes the results and findings of Mid-America Transportation Research Center (MATC) research project No. 59709. It is focused on the measurement of strain and temperature in concrete structures during or after exposure to high temperatures using pulse pre-pump Brillouin optical time domain analysis (PPP-BOTDA). The main objectives of this study are: (a) to study the strain transfer in concrete after exposure to high temperatures using PPP-BOTDA based fiber optic sensors; (b) to apply distributed fiber optic sensing (DFOS) technology based on PPP-BOTDA in small-scale steel-concrete composite slabs for temperature measurement; (c) to apply distributed fiber optic sensing (DFOS) technology based on PPP-BOTDA in large-scale concrete slabs for temperature measurement. Dog-bone shaped ultra-high performance mortar was fabricated with DFOS embedded. They were subjected to different high temperatures and then natural cooling. After that, they were tested under tension. PPP-BOTDA based strain results compared well with the strain gauge data taken from the test. This test demonstrates the effectiveness of strain transfer between the fiber optic sensors and concrete after exposure to high temperatures due to the occurrence of melting residues which provide friction between them. Six 1.2 m × 0.9 m steel–concrete composite slabs were instrumented with DFOS and thermocouples subjected to fire for over 3 h. Dense point clouds of temperature in the slabs were measured using DFOS. The test results show acceptable accuracy using DFOS for structural fire applications and non-uniform three-dimensional temperature distributions in steel–concrete composite slabs. Several large-scale composite floor beams were fabricated and tested under mechanical or combined mechanical and fire conditions. The concrete slabs were instrumented with DFOS technology in an attempt to measure temperature distribution. Comparisons with co-located thermocouples show that while the increased spatial resolution

provides new insights about temperature phenomena, challenges for local temperature measurements were encountered during this first attempt at application to large-scale specimens.

Chapter 1 Introduction

Concrete and steel materials have been widely used in civil engineering to construct infrastructures to improve the quality of life. An unintentional fire could become one of the most severe hazards during engineering structures' lives. Among different infrastructures, bridges are extremely vulnerable to fire, which is usually caused by crashing trucks and burning combustible materials near the bridge. Bridge fire can result in significant economic losses due to the disruption of traffic in the fire region. Also, severe hydrocarbon fires with high temperatures and fast heating rates due to burning gasoline can lead to a great threat and damage to the bridge members and even collapse of the bridge after exceeding the fire resistance. Suitable fire safety measures are needed for infrastructures (such as bridges and buildings) to minimize the property loss and maintain the structural performance in terms of heat transfer, stability, and integrity (Garlock et al. 2012).

During or after the exposure of engineering structures to fire or high temperatures, it is useful to collect sufficient strain and temperature data of heated engineering structures. In this way, the structural conditions can be well monitored in-situ and the collected information can be used to further evaluate the residual life and to determine if the structures need repair or demolition. A quick and effective decision from practicing engineers and researchers based on the useful data is invaluable to reduce economy losses and refresh the structural functions immediately after a fire event.

However, it is still very challenging to measure strain and temperature data under or after exposure to high temperatures. Strain gauges have been widely used to measure strains at different single points under ambient temperature, but several technical issues arise during high-temperature measurements. Challenges involve finding a material which can be thermally stable

at high temperatures to fabricate strain gauges. Another is to find an effective bonding material which can be used to attach strain gauges to the host structure. For example, the maximum operational temperatures of epoxy bond materials used to bond the steel and concrete are approximately 400℃ and 100℃, respectively. Until now, the performance of stain gauges used in fire conditions is not reliable. On the other hand, thermocouples are a mature temperature measurement technology, having known temperature measurement uncertainty. However, it has two drawbacks. One is using a wiring to connect the data acquisition with each thermocouple. The other is hundreds of thermocouples needed to measure gas and structural temperatures in a fire test.

Recently, fiber optic sensors for temperature and strain measurements have attracted attention among the fire research community. Fiber optic sensors have been widely used to monitor strains in engineering structures (concrete, cables, and pavement, etc.) during construction or curing and full-life health monitoring at ambient temperatures. In the late 1990s, fiber optic sensors have started to measure strains or temperatures up to 300℃ (Inaudi and Glisic, 2006). Usually, fiber optic sensors have a glass core which has a transition temperature of 1200℃. A cladding, which has low refractive index, forms outside the glass core to prevent abrasion and moisture attack to the glass core. Coatings are covered on the cladding to provide strength and extend service life of fiber optic sensors. Note that most coatings usually have a melting temperature of approximately 300℃. Therefore, Bao et al. (2016a) calibrated a pulse pre-pump Brillouin optical time domain analysis (PPP-BOTDA) based distributed fiber optic sensor up to 800℃ in the laboratory test, which only included the glass core and cladding. The principle of fiber optic sensors to measure strain and temperature includes three types of light scattering: Rayleigh, Brillouin, and Raman scattering. When a light travels into an optical fiber,

it can be scattered because the light (i.e., photons) interacts with the crystal micro-structures of the optical fiber. Rayleigh scattering is a kind of elastic scattering signal which has the same wavelength as the light. Brillouin and Raman scattering are inelastic scattering signals which has Stokes and anti-Stokes signals. Fiber optic sensors used for strain and temperature measurements typically includes Extrinsic Fabry-Perot Interferometer (EFPI), Fiber Bragg Gratings (FBG), Long Period Fiber Grating (LFBG), and distributed fiber optic sensing (DFOS).

In this study, DFOS was used to measure strain and temperature of concrete structures exposure to high temperatures or fire. It has already been noticed that, when using DFOS to measure strain, DFOS needs to be adhered on the surface of steel or concrete members or embedded inside. Therefore, the bond between the distributed fiber optic sensors and the host structure is a critical technical issue at elevated temperatures. Also, their different material properties and thermal expansion coefficients must be taken into account when measuring the strain at elevated temperatures. A reliable attachment method between them is needed and the strain transfer between them should be stable and characterized. For temperature measurement, the distributed fiber optic sensors must be free of strain in concrete structures. The sheath outside the tight buffer covered on the coating can make the fiber core freely shrink or expand at the ambient temperature. However, after exposure to high temperatures or fire conditions, the sheath and buffer would be melted. The heated material residues might bridge the cladding of the fiber and host concrete structure. The question remains whether it is still strain free for DFOS to measure temperature. To this end, this study explores the strain transfer between distributed fiber optic sensors and concrete after exposure to high temperatures. Also, distributed fiber optic sensors are used to measure temperature distribution in small and large-scale concrete slabs to validate feasibility of measurement approaches.

Chapter 2 Distributed Fiber Optic Sensor Calibration for Temperature Measurement

The distributed fiber optic sensor (DFOS) used in this study was a simplex fiber optic cable composed of a polymer sheath, an aramid yarn, and an optical fiber, as illustrated in Figure 2.1(a) and (b). The optical fiber had a buffer (outer diameter: 880 μm), an outer coating (outer diameter: 242 μm), an inner coating (outer diameter: 190 μm), a glass cladding (outer diameter: 125 μm), and a glass core (diameter: 8.2 μm). The buffer and coatings were composed of mixtures of monomers, oligomers, photo-initiators, and additives and used to protect the glass from mechanical impact, and abrasion/environmental exposure, respectively. According to preliminary testing, after the fiber optic cable was embedded in the concrete slab, the optical fiber was free to slide in the sheath with negligible friction so that it was essentially free of axial strain over the relatively short fibers used in this study. Thus, the DFOS can be used to measure temperature changes (Bao and Chen 2015). The DFOS used in this study to measure strain change does not have the polymer sheath and aramid yarn and other components since the strain DFOS are the same as the temperature sensor. As illustrated in Figure 2.2, the optical fiber formed a closed loop with a data acquisition system and served as a light transmission cable in addition to sensing. The data acquisition system was set to sample points every 1 cm over a measurement distance of up to 200 m so the temperature of two points spaced at no less than 2 cm could be distinguished. The instrument was about 10 m away from the specimen during the fire testing. The measurement from the optical fiber was made using a designated instrument, the Neubrescope® (model: NBX-7020), based on Brillouin scattering, as elaborated in a prior study (Bao and Chen 2015). The instrument measured the temperature-dependent Brillouin frequency shift along the fiber optic cable. In this study, the scanning frequency was swept from 10.82 GHz to 11.67 GHz, which corresponded to an approximate temperature range of 20 °C to 1100 °C

(Bao and Chen 2015). The relationship between the Brillouin frequency shift and temperature was calibrated in prior studies, as elaborated in Bao and Chen (2016). The sensitivity coefficients were determined using a tube furnace with computer-controlled temperature. The calibration relationship is shown in Equation 2.1:

$$\Delta\nu_B = (-3.464 \times 10^{-7}T + 1.110 \times 10^{-3})(T - 22) \quad (2.1)$$

where $\Delta\nu_B$ denotes the Brillouin frequency shift (GHz); and T denotes temperature (°C).

Additional information about the Brillouin scattering technique and fiber calibration are provided in (Bao 2017).

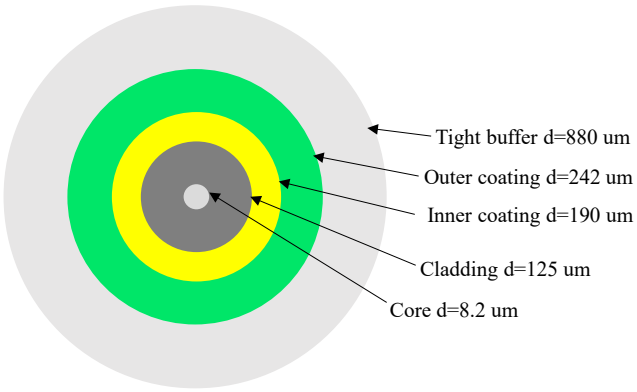

(a)

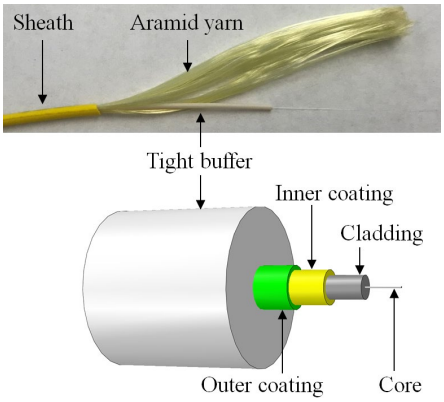

(b)

Figure 2.1 Single-mode optical fiber used as strain and temperature sensors: (a) overall composition excluding the aramid yarn and sheath and (b) photo of cross section with annotation (not to scale)

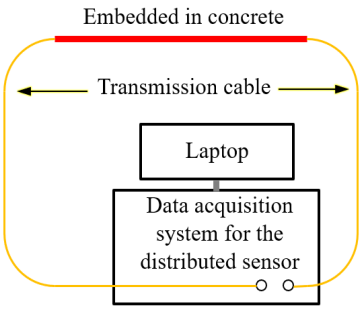

Figure 2.2 Schematic of measurement setup using distributed fiber optic sensor (a length of the fiber optic cable embedded in the concrete specimen)

Chapter 3 Strain Measurement of Ultra-high Performance Mortar After Exposure to High Temperatures

3.1 Introduction

In civil engineering, strain measurement could provide valuable information for the evaluation of health status of engineering structures in operation. Commonly, strain gauges are used in the lab and field tests to capture the deformation at one point. However, strain gauges only provide single-point strain values and the adhesive used to glue the strain gage with the host structure (such as steel and concrete etc.) cannot sustain high temperatures, which limits the application of strain gauges. To capture structural strain under fire conditions is extremely challenging. To date, strain measurement under high temperatures up to 1000℃ has been rarely studied in literature.

Huang et al. (2010) developed a temperature self-compensated long-period fiber-grating (LPFG) sensor for large strain measurement at high temperatures. The effect of the elastic attachment and gauge length change on the strain and temperature sensitivities of the LPFG sensors, as well as the strain transfer ratio, was investigated. The LPFG sensor can work at a temperature of 700℃ with a strain up to 1.5%. Liu et al. (2016) developed a strain measurement at high temperature based on the Fabry-Perot interferometer cascaded fiber regeneration grating. The experimental results show the proposed sensor can simultaneously measure strain (0-600$\mu\varepsilon$) and temperature (19-600℃). Bao et al. (2016c) used a fiber optic strain sensor to measure the strain of steel beams subjected to fire. The concept of the fiber optic sensor developed stems from Huang et al. (2010). The results showed the average error between the measured strain and simulated strain was less than 13%. From previous studies, it can be seen these fiber sensors only

provide point values, although they could survive at a high temperature. Meanwhile, they were installed on the surface of structures to measure strain at high temperatures.

In the present study, the aim is to investigate the feasibility of strain measurement using the distributed fiber optic sensors. The distributed fiber optic sensors were embedded inside the cement mortar which was exposed to high temperatures and then subjected to natural cooling immediately. The bond between the distributed fiber optic sensor and the cement mortar after exposure to high temperature as well as the strain transfer between them were verified. Although the strain measured in this study is not under high temperature, strain measurement using distributed fiber optic sensors embedded inside structures after exposure to high temperature is still desirable. The strain information can be used to evaluate structural post-fire performance or residual life and provide the fire scientist a solid basis for determination if a suitable strengthening strategy is needed.

3.2 Specimen Preparation

Small scale tests were conducted to characterize the strain transfer to the fiber optic sensors embedded in concrete exposure to high temperatures. Dog-bone specimens were fabricated. The ultra-high performance mortar was cast into a standard mold and after 24 hours the specimens were demolded. Then, the specimens were cured for 28 days in the saturated $Ca(OH)_2$ solution after being demolded at one day. The parameters for the tested specimens are shown in Table 3.1. Five groups of specimens (corresponding to 22℃ (ambient temperature), 250℃, 350℃, 450℃ and 500℃) were fabricated with the same dimensions and each group has three specimens. All test specimens were put into a furnace to dry for three hours at a temperature of 100℃ to avoid spalling when later exposed to high temperatures. The used furnace and temperature controller are shown in Figure 3.1(a).

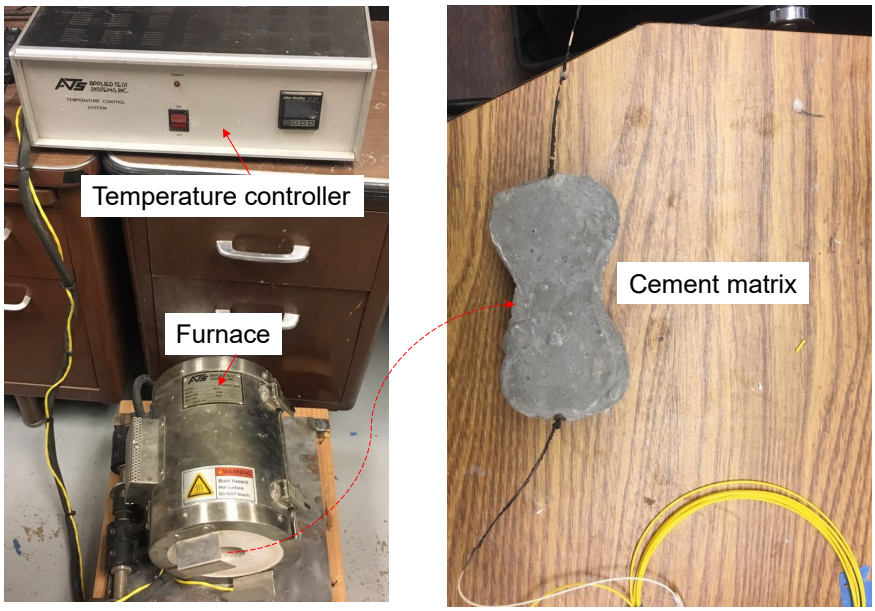

(a) (b)

Figure 3.1 (a) Furnace and temperature controller (b) Cement matrix after 350℃

Table 3.1 Parameters for Tested Specimens

Specimens ID	Temperature (℃)	Maintenance time (hours)
22	22	3
250	250	3
350	350	3
450	450	3
500	500	3

After natural cooling, three specimens were tested under tension at the ambient temperature to verify the effectiveness of strain transfer at the ambient temperature. The other four groups of specimens were first heated up to 250℃, 350℃, 450℃ and 500℃, respectively, and the temperature was maintained for three hours before cooling naturally. The specimen after a high temperature of 350℃ is shown in Figure 3.1(b). After, the specimens were put into the testing frame.

3.3 Material Properties

In the present study, ultra-high performance mortar was used to fabricate these specimens. The mixture proportions are listed in Table 3.2.

Table 3.2 Mixture Proportions for Ultra-high Performance Mortar

Constituents	**Amount (g/3L)**
Cement	1986
Silica fume	126
Fly ash class C	1239
River sand	1581
Masonry sand	924
Light weight sand	360
High-range water reducer	35
Air detrainer	26.8
Water	621

Note: High-range water reducer is based on polycarboxylate; the slump of the ultra-high performance mortar was 280 mm.

3.4 Testing Method and Instrumentation

The briquette tension test was carried out to investigate the bond performance between the mortar and distributed fiber optic sensors. Usually, the direct tensile strength of cement mortar can be tested by the briquette tension test described in AASHTO T132 (2018). The dog-bone shaped briquette is 75 mm long and 25 mm thick. The minimum cross section (i.e., at mid length) of the briquette is 625 mm^2. The dimensions of the briquette are shown in Figure 3.2(a). The distributed fiber optic sensor was embedded in the center along the length direction of the specimen during casting ultra-high performance mortar. A strain gauge was adhered on the surface of the specimen at mid length prior to the test. Figure 3.2(b) shows a testing specimen.

The testing frame (Instron 5965) with a load capacity of 100 N was used to test the specimen. The maximum data acquisition rate of the testing frame for load, extension and strain is 2500 Hz. The testing frame could automatically record the load and extensometer. The extension is approximately equal to the frame movement and neglects the small elastic deformation of the steel grip. The accuracy of measured load is ±0.5% of reading. The displacement rate of the testing frame varies between 0.001 and 3000 mm/min. In the present study, the displacement of the crosshead of the testing frame was controlled during loading and a displacement rate of 0.5 mm/min was chosen to achieve static loading. Figure 3.2(b) and (c) also show the strain measurement using PPP-BOTDA and strain gauge acquisition, respectively.

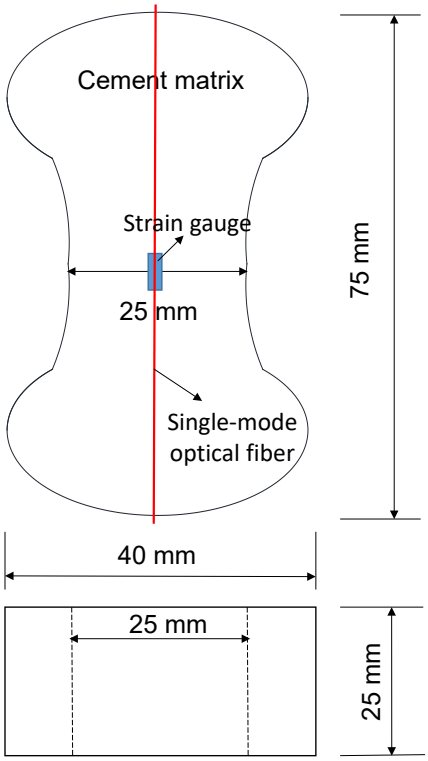

(a)

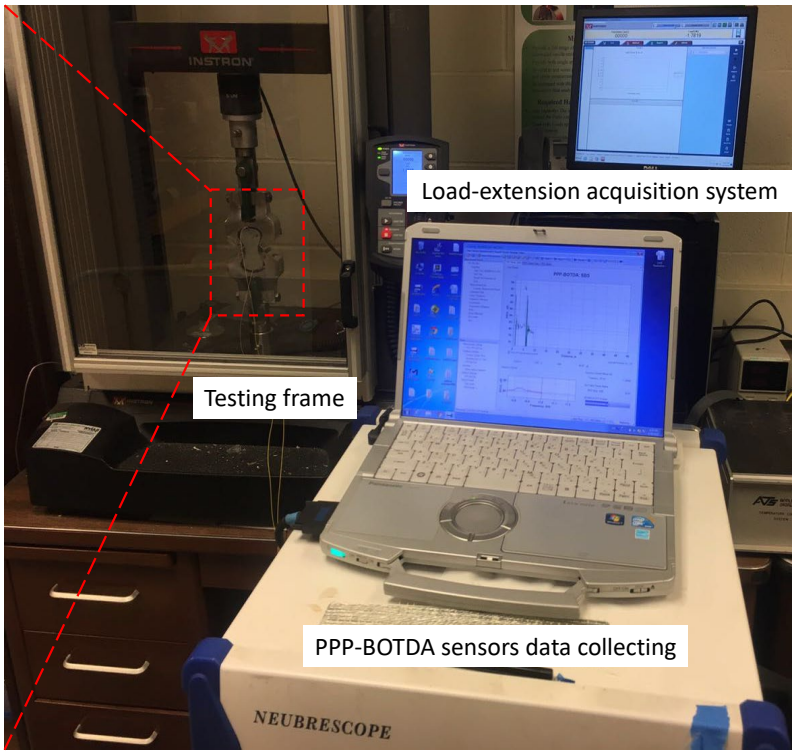

(b)

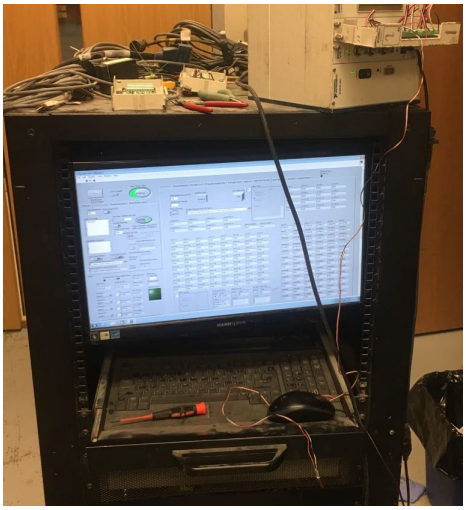

(c)

Figure 3.2 (a) Dimensions of specimen (b) testing setup and measurements (c) data acquisition for strain gauge

3.5 Results and Discussion

Figure 3.3(a) and (b) show the typical failure mode of the cross section of two kinds of specimens. The optic fiber cross-section can be seen on the overall specimen cross-section. The fiber in the '22' specimen shows no damage in Figure 3.3(a) while the fiber in the '350' specimen showed a black channel in Figure 3.3(b). However, the burning residuals still provide friction between the cement matrix and fiber, which is evidenced from the measured strains by PPP-BOTDA. Figure 3.4 shows load-extension curves. The high temperature affects the tensile strength and does not have much influence on the extension. The maximum extension is about 1.0 mm for all tested specimens. All the specimens reach the maximum load, suddenly followed by brittle failure. Also, the specimen exposure to 250℃ has the highest strength among all tested specimens. This is because a certain degree of temperature could increase the hydration degree of cement matrix and thus enhance the strength. After the temperature increases to higher than 250℃, the strength gradually decreases.

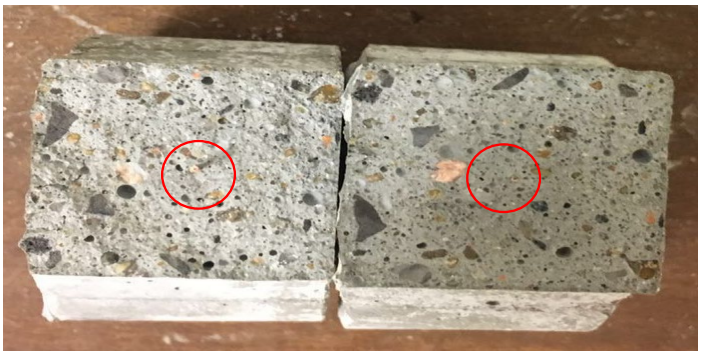

(a)

(b)

Figure 3.3 Typical failure mode of cross section (a) 22 specimen (b) 350 specimen (red circles in images indicate the fiber location approximately)

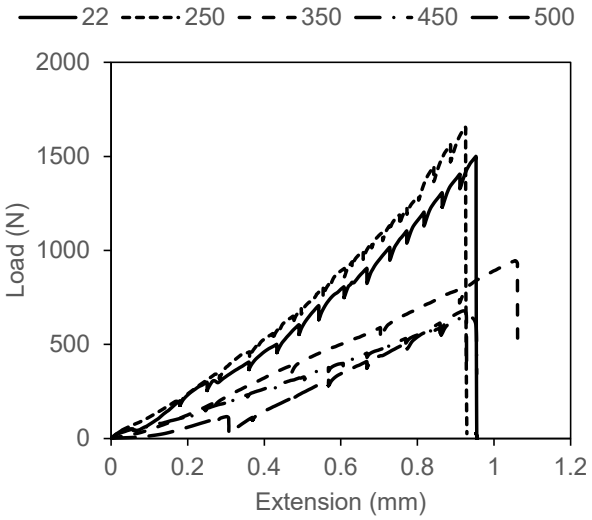

Figure 3.4 Load-extension curves

Figure 3.5(a) shows the strain development versus load of the specimens after exposure to different temperatures. Each curve has a fitting equation provided in the figure. At the ambient temperature, the relationship between the load and strain is linear. However, as the temperature increases, the relationship between them becomes nonlinear. Also, the nonlinear relationship is more easily visible at a smaller load as the temperature increases. Figure 3.5(b) shows the strain development versus exposed temperatures at different loads. The load is limited to 600 N because the specimens exposed to more than 250℃ cannot carry a load of more than 600 N. Similarly, the nonlinear relationship between the strain and temperature becomes more evident at a higher load. Before 200℃, the strain almost linearly develops with the temperatures.

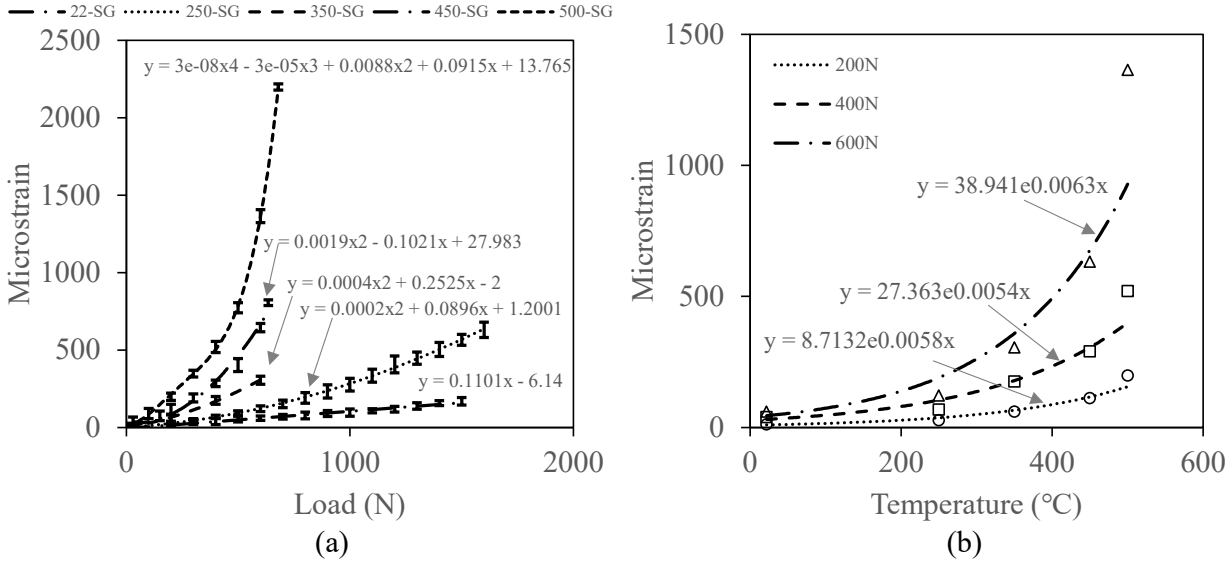

Figure 3.5 (a) Strain gage data versus load after different temperatures (b) strain gage data versus temperature at different loads

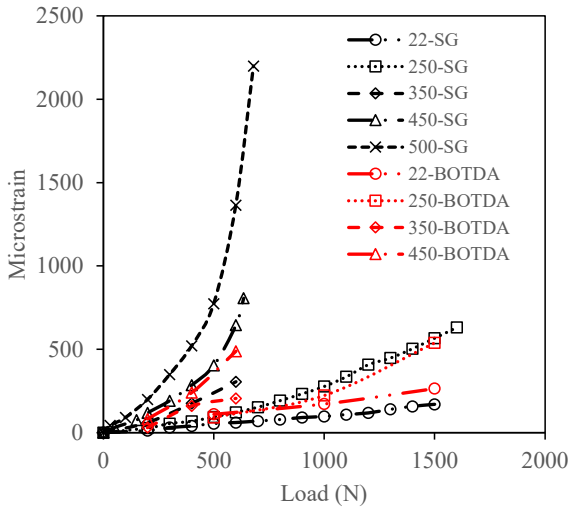

Figure 3.6 Strain comparisons between BOTDA sensors and strain gages after different temperatures

Table 3.3 Strain Data Collected by PPP-BOTDA Sensors

Load(N)/Specimens	22	250	350	450
0	728.2/54.8	728.1/79.3	104.3/67.5	555.6/77.4
200	-	-	134.0/110.6	637.8/74.3
400	-	-	264.6/77.8	795.3/64.7
500	838.1/76.4	818.6/61.6	-	-
600	-	-	309.1/96.0	1044.1/104.1
1000	900.3/75.7	950.3/92.5	-	-
1500	992.6/72.8	1266.0/72.8	-	-

Note that values in table include absolute strain value and standard deviation.

Table 3.3 shows measured strain results from PPP-BOTDA sensors. For each specimen after exposure to high temperature, the strains obtained from PPP-BOTDA sensors nonlinearly increase with the load. The strain increment becomes larger at higher load levels. Also, a higher temperature results in more damage on the specimen (such as voids and microcracks inside). Thus, the specimen after exposure to high temperatures would be subjected to higher strain under

the same load due to the reduction of stiffness. Figure 3.6 shows strain comparisons between PPP-BOTDA sensors and strain gauges. It should be noted PPP-BOTDA sensors do not have readings at the temperature of 500℃ because of the broken fiber. The comparison between the PPP-BOTDA sensors and strain gauges at the temperature of 500℃ is not available. Their strain results are comparable after exposure to 250℃, 350℃, and 450℃ for three hours. This means that strain transfer from concrete to the optical fiber can be achieved after high temperatures.

3.6 Summary

Strain inside the cement mortar after exposure to high temperatures was measured by PPP-BOTDA based fiber optic sensors. The PPP-BOTDA measured strain was compared with the results obtained from strain gauges. The comparison indicates the strain transfer from concrete to the optical fiber can be achieved after exposure to high temperatures.

Chapter 4 Measuring Three-Dimensional Temperature Distributions in Steel–Concrete Composite Slabs Subjected to Fire Using Distributed Fiber Optic Sensors

4.1 Introduction

Material temperature distribution can play a significant role in the safety and durability of civil engineering structures. During normal operation, temperature affects the energy efficiency of the building (Moroşan et al. 2010) and large temperature gradients can generate or aggravate internal stresses that may cause damage (Li et al. 2017). The damage induced by thermal effects can be particularly critical in large concrete structures, such as dams, because of the significant heat released during the cement hydration process (Meng et al. 2018). During an extreme event, such as a building fire, the mechanical properties of construction materials and the load-carrying capacity and stability of structural members (beams, columns, slabs, and joints) are reduced at elevated temperatures (Kodur et al. 2010; Lamont et al. 2007). Therefore, it is of great importance to assess the temperature distribution of structures at different stages of their life cycle. In this paper, we focus on measurement in fires.

In the literature, methods to assess material temperature distributions during a fire can be grouped into two categories. The first category is based on computer simulations of fire dynamics and heat transfer to predict temperature distributions in structures (Bundy et al. 2007). Typically, thermodynamic analysis of the fire is performed and followed by heat transfer analysis to the structure to predict the temperature distribution and evolution. Then, a thermo-mechanical analysis is often performed to analyze the mechanical response of the structure. A number of analytical and numerical tools have been developed to predict gas-phase temperature distributions and evolution histories resulting from fire. Computational fluid dynamics models (McGrattan et al. 2010) or stochastic models (Bertola et al. 2009) are often used. Despite these

advances, it remains a challenge to accurately predict temperature distributions in structural members using the heat transfer analysis based on gas temperatures and radiative heat flux, particularly for structures with complex geometry such as composite floors (Ramesh et al. 2019). The error in the predicted structural member temperature distribution and evolution over time may result in inaccurate conclusions about the mechanical response of the structure. Additionally, the uncertainty in structural element temperature distribution cannot easily be quantified.

The second category of methods is based on the physical measurement of temperature. Infrared cameras can image temperature distributions on the surface of structures (Hoehler et al. 2016). With the recent advent of robotic platforms, such as various unmanned vehicles, infrared cameras have become more attractive for use in hazardous applications. However, infrared cameras only provide measurement of temperature at the visible surface, and cannot measure the internal temperature, which is also important. For instance, the internal temperature of concrete may significantly affects the bond strength between steel and concrete (Li et al. 2017). In current practice, the internal temperature in concrete is frequently measured using thermocouples. Each thermocouple monitors a single point where the thermocouple junction is located. Numerous thermocouples are thus needed to monitor a large structure (Li et al. 2019).

Recently, various fiber optic sensors have been developed for structural fire applications. These include fiber Bragg grating (FBG) sensors, long-period fiber grating (LPFG) sensors, interferometer sensors, and distributed fiber optic sensors (Bao et al. 2019). FBG sensors and LPFG sensors are manufactured by inscribing gratings (i.e., periodic change of the refractive index) in optical fibers. The gratings change if the fiber is subjected to environmental variations, e.g., changes in fiber temperature. For example, FBG sensors were used to measure gas

temperatures up to 300 °C in a scaled (1:20) tunnel (Lonnermark et al. 2008). However, conventional FBG sensors are prone to thermal degradation and have a maximum operation temperature of about 350 °C (Bao et al. 2019). Regenerated FBG (rFBG) sensors have been developed using a sophisticated fabrication process to improve the thermal stability of the grating and have been applied to reinforced concrete beams in fire testing to measure temperatures higher than 900 °C (Rinaudo et al. 2015). Compared with conventional FBG sensors, LPFG sensors have demonstrated better thermal stability, and have been used to study steel frames subjected to elevated temperatures (Huang et al. 2013). The LPFG sensors measured temperatures up to 800 °C. Additionally, various interferometer sensors have been developed to measure temperature and strain in high temperature applications (Bao et al. 2019). Among them, extrinsic Fabry–Perot interferometer sensors have been used, specifically in structural fire testing (Bao et al. 2016d) to record temperatures up to about 1000 °C. Grating sensors and interferometer sensors provide measurements at discrete points, while distributed sensors provide continuous measurements along the length of an optical fiber without the need for gratings. For example, a single optical fiber was used to obtain continuous measurement along the entire length of a concrete cylinder (Bao et al. 2015). In addition to the capability of continuous measurement, a distributed fiber optic sensor utilizes a telecommunication-grade single-mode optical fiber, which serves as both the distributed sensor and the transmission line, making the sensor inexpensive; less than $0.50 USD per meter. Moreover, the distributed sensors eliminate the need for fabrication of gratings or interferometers using special equipment. However, the initial cost of the data acquisition system is often higher than that of the other fiber optic techniques.

If temperatures in structural members during a fire can be measured with sufficient spatial resolution, analyzing the structural response due to thermal loading will become more tractable. Recently, distributed fiber optic sensors have proven feasible to measure temperature and strain at high temperatures (Bao and Chen 2016 a and b). Other distributed sensors have been used to measure temperatures in small-scale steel and reinforced concrete beams subjected to fire. For example, temperature distributions of a small steel beam exposed to combined fire and mechanical loading were measured and enabled an enhanced thermal–mechanical analysis of the steel beam (Bao et al. 2016c); In addition, temperature distributions in a small reinforced concrete beam exposed to fire were measured and enabled detection of cracks in the concrete (Bao et al. 2017b). Based on the existing studies, it is rational to hypothesize that distributed fiber optic sensors can be deployed in structures to image three-dimensional temperature distributions and generate digital models of these distributions.

This study has three objectives: (1) develop a method to image three-dimensional temperature distributions in concrete members; (2) develop a method to install distributed sensors following a procedure feasible for building construction practice; and (3) implement and evaluate the methods in six small steel–concrete composite slabs to understand their response under severe fire conditions. The measurements are used to generate three-dimensional information on temperature fields in the concrete and compare them with temperatures measured using co-located thermocouples and an infrared camera. The remainder of the study is organized as follows: Section 4.2 introduces the experimental program, including the specimens and material properties, instrumentation, test setup, and fire testing protocol; then, Section 4.3 presents and discusses the experimental results; finally, Section 4.4 summarizes the new findings from this research.

4.2 Experimental Program

4.2.1 Specimens and Material Properties

Table 4.1 summarizes the six composite specimens (CS), designated as CS-1 to CS-6, fabricated to develop the installation scheme of distributed fiber optic sensors (DFOS) in concrete and investigate the response of the distributed sensors to fire-induced temperature increase in concrete. Each DFOS system is compared with a number of thermocouples (TCs) to validate its accuracy. Each specimen consisted of a reinforced concrete slab supported on two W5×19 steel beams, as depicted in Figure 4.1(a). Composite action between the concrete slab and steel beams was achieved using headed steel studs. It is noted that although the number of headed studs varied (four or six), this did not play a significant role in this study.

Each concrete slab was 1219 mm long and 914 mm wide and cast on 0.9 mm thick, trapezoidal metal decking (Vulcraft 3VLI20), which served as a stay-in-place formwork. Consequently, the depth of the concrete slab varied from 83 mm to 159 mm, as illustrated in Figure 4.2(b). The concrete slab was reinforced with welded wire mesh (6 × 6, W1.4/W1.4), which had a specified mesh spacing of 150 mm and a wire diameter of 3.4 mm. The headed steel studs had a specified shaft diameter of 19 mm and an effective embedment length of 117 mm. The two W5×19 steel beams were 1829 mm long and placed parallel with 610 mm spacing.

Each steel–concrete composite specimen was fabricated as follows:

- Each end of the two parallel steel beams was connected by a perpendicular, welded rectangular steel tube so the beams maintained their position during fabrication.
- A 1219 mm × 914 mm rectangular wood formwork was prepared.
- The trapezoidal metal decking was laid on top of the beams inside the formwork.

- The headed studs were welded through the metal decking to the steel beams (Figure 4.1).
- The welded wire mesh was supported by plastic chairs 8 mm above the metal decking.
- Optical fibers and thermocouples were deployed as detailed in Section 4.2.
- Concrete was poured into the formwork. Concrete placement using a hand trowel as well as placement directly from the chute on the concrete truck was used.
- The sides of the formwork were tapped using a rubber mallet to consolidate concrete at the edges; no mechanical vibrators were used.
- The cast specimen was covered under wet burlap and a plastic sheet, demolded after 1 day, and cured at room temperature (22 °C ± 3 °C).

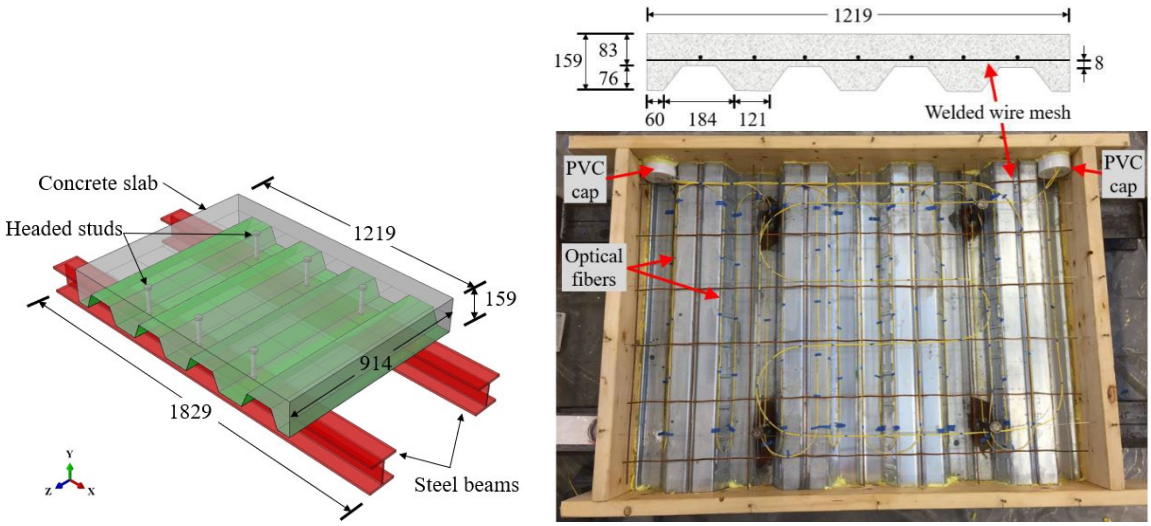

(a) (b)

Figure 4.1 Steel–concrete composite slab specimens (units in mm): (a) isometric rendering, and (b) cross-sectional and top views. The yellow cables are the optical fibers.

The concrete mix was 0.193: 0.105: 0.315: 1.0: 1.136 by mass for water : Class C fly ash : Type I Portland cement: river sand : expanded slate lightweight aggregate (LWA). With a binder composed of 25% fly ash and 75% Portland cement, this mix corresponded to a water-to-binder ratio of 0.46. The river sand had a diameter up to 4.75 mm. The lightweight aggregate used had low water-retention characteristics and high desorption (Pour-Ghaz et al. 2012; Meng et al. 2017 and 2018). The river sand and lightweight aggregate were prepared to ensure the saturated-surface-dry condition. A polycarboxylate-based high-range water reducer was used to improve flowability of the concrete. The dosage of the water reducer was adjusted to achieve a specified slump of 220 mm to ensure adequate consolidation during casting. Polypropylene monofilament microfibers (FRC MONO-150 ®) with a nominal diameter of 38 μm and length between 13 mm and 19 mm were added to the mix at a dosage of 2.37 kg/m^3 of concrete to reduce temperature-induced spalling (Maluk et al. 2017). The concrete was mixed at a local batching plant and transported less than 10 min to the test facility for casting.

During concrete casting, ten standard cylinders measuring 102 mm in diameter and 203 mm in height were prepared for concrete material testing. Five cylinders were tested and analyzed to determine the average ± standard deviation of each concrete property. Specifically, the concrete density was 2070 ± 80 kg/m^3 at 28 days. The compressive strength of concrete was 38 ± 3 MPa at 28 days and 41 ± 3 MPa at 56 days, which were determined in accordance with the American Society for Testing and Materials (ASTM) C39/C39M. A relative humidity sensor (Vaisala HM40S RH Probe) was inserted into each concrete slab to measure the internal relative humidity of concrete at a depth of 90 mm. The internal relative humidity measured shortly before the fire test is listed in Table 4.1. Table 4.2 lists the nominal tensile yield strength (f_y), the

ultimate strength (f_u), and the modulus of elasticity (E) of various types of steel adopted in this study, as specified by the manufacturers.

Table 4.1 Details of the Composite Specimens

Designation	Age at Testing (days)	Internal Relative Humidity before Test	Number of Studs	Distributed Sensors	Thermocouples
CS-1	33	94.3%	6	DFOS-1 to DFOS-3	TC1 to TC6
CS-2	34	93.5%	6	DFOS-1 to DFOS-3	TC1 to TC6
CS-3	35	95.0%	4	DFOS-1 to DFOS-3	TC1 to TC6
CS-4	36	95.2%	4	DFOS-1 to DFOS-3	TC1 to TC6
CS-5	350	77.7%	4	DFOS-1 to DFOS-4	TC1 to TC6; ST1 * to ST9
CS-6	351	78.6%	6	DFOS-1 to DFOS-4	TC1 to TC6; ST1 to ST9

* "ST" stands for "surface thermocouples".

Table 4.2 Nominal Mechanical Properties of Steel Used in Composite Specimens

Steel Used in the Specimens	ASTM Material Standards	Tensile Yield Strength (MPa)	Ultimate Strength (MPa)	Modulus of Elasticity (GPa)
Beams	A992 (structural steel)	345	450	200
Headed studs	A108 (cold drawn)	414	496	205
Welded wire mesh	A185 Grade 65	448	517	200
Galvanized metal decking	A611 Grade D (cold rolled)	276	359	203

4.2.2 Instrumentation

Figure 4.2 shows the deployment of the sensors. Specimens CS-1 to CS-4 were instrumented with three distributed fiber optic sensors (DFOS-1 to DFOS-3) each. Specimens CS-5 and CS-6 had an additional distributed fiber optic sensor (DFOS-4) on the top surface. DFOS-1 was laid directly on top of the metal decking along its flutes, which is perpendicular to the steel beams. DFOS-2 was attached on top of the welded wire mesh and also parallel to the flutes of the specimen. DFOS-3 was also attached on top of the welded wire mesh but ran perpendicular to the flutes of the specimen. For reference, the curved portions of the distributed sensors were labeled as B1 to B14 for sensor DFOS-1, T1 to T7 for sensor DFOS-2, and L1 to L4 for sensor DFOS-3. The two sensors running transverse to the steel beams (DFOS-1 and DFOS-2) entered the concrete from a polyvinyl chloride (PVC) cap at Point A, and the longitudinal sensor DFOS-3 entered the concrete from a PVC cap at Point C. Each cap measured 100 mm in diameter and was used to store the lengths (500 mm) of each distributed sensor at the two ends during concrete casting and transport of the specimens. The gap between the cup and formwork was small enough to prevent the leaking of concrete. The cup provided mechanical protections and ensured the distributed sensors were free from the concrete. After the specimens were demolded, the length of each distributed sensor stored in the cup was connected to the data acquisition system for measurement. Sensor DFOS-4 was attached on the top surface of the concrete after the concrete was cured for one year. A thin groove (depth ≈ 3 mm) was cut into the concrete using a grinding wheel to accommodate the optical fiber and a thin layer (≈1 mm) of cement mortar was used to cover the sensor. The distributed sensor passed across the specimen in six paths perpendicular to the flutes of the slab, denoted by Path I to Path VI, as shown in

Figure 4.2(e). All optical fiber turns had a radius larger than 50 mm, which is adequate to avoid any significant light signal attenuation.

Figure 4.2 also shows thermocouples “TC” embedded in the concrete and thermocouples “ST” attached on the top surface of the concrete slab. In specimens CS-1 to CS-4, each specimen was instrumented with six glass-sheathed, bare bead, K-type thermocouples (24-gauge wire), designated as TC1 to TC6. TC1 was located on the top surface of the metal decking in the center of the specimen. TC2 was on the welded wire mesh in the center of the specimen. TC3 was on the welded wire mesh 305 mm away from the mid-span. TC4 was on a headed stud 300 mm away from the mid-span. TC5 and TC6 were peened into a small drill hole (diameter: 1.5 mm) in the center bottom flanges of the two steel beams. An additional Inconel-shielded thermocouple located 25 mm below the metal decking at the center of the compartment was installed to measure the gas temperature just below the concrete deck. In specimens CS-5 and CS-6, each specimen was instrumented with nine additional thermocouples on the top surface of the concrete slab, designated as ST-1 to ST-9 in Figure 4.2(e). All the thermocouples have a manufacturer-specified temperature standard limit of error of 2.2 °C or 0.75% (whichever is greater) over a measurement range of 0 °C to 1250 °C. The total expanded uncertainties (coverage factor of 2) for the material temperature and gas temperature measurements are ± 6.2% and ± 14.7% of the reading, respectively. The total expanded uncertainty for the burner heat release rate is less than ± 2.4% (Bryant and Bundy 2019). The distributed optic fiber sensors have an estimated expanded uncertainty of ± 11.2% of the reading. Data from the fuel delivery system and thermocouples were recorded at a rate of 1 Hz.

In addition to the fiber optic sensors and thermocouples, a high-speed mid-wavelength infrared camera (FLIR SC8300HD ®) was used to image the surface temperature of select specimens, with emphasis on the top surface of each concrete slab.

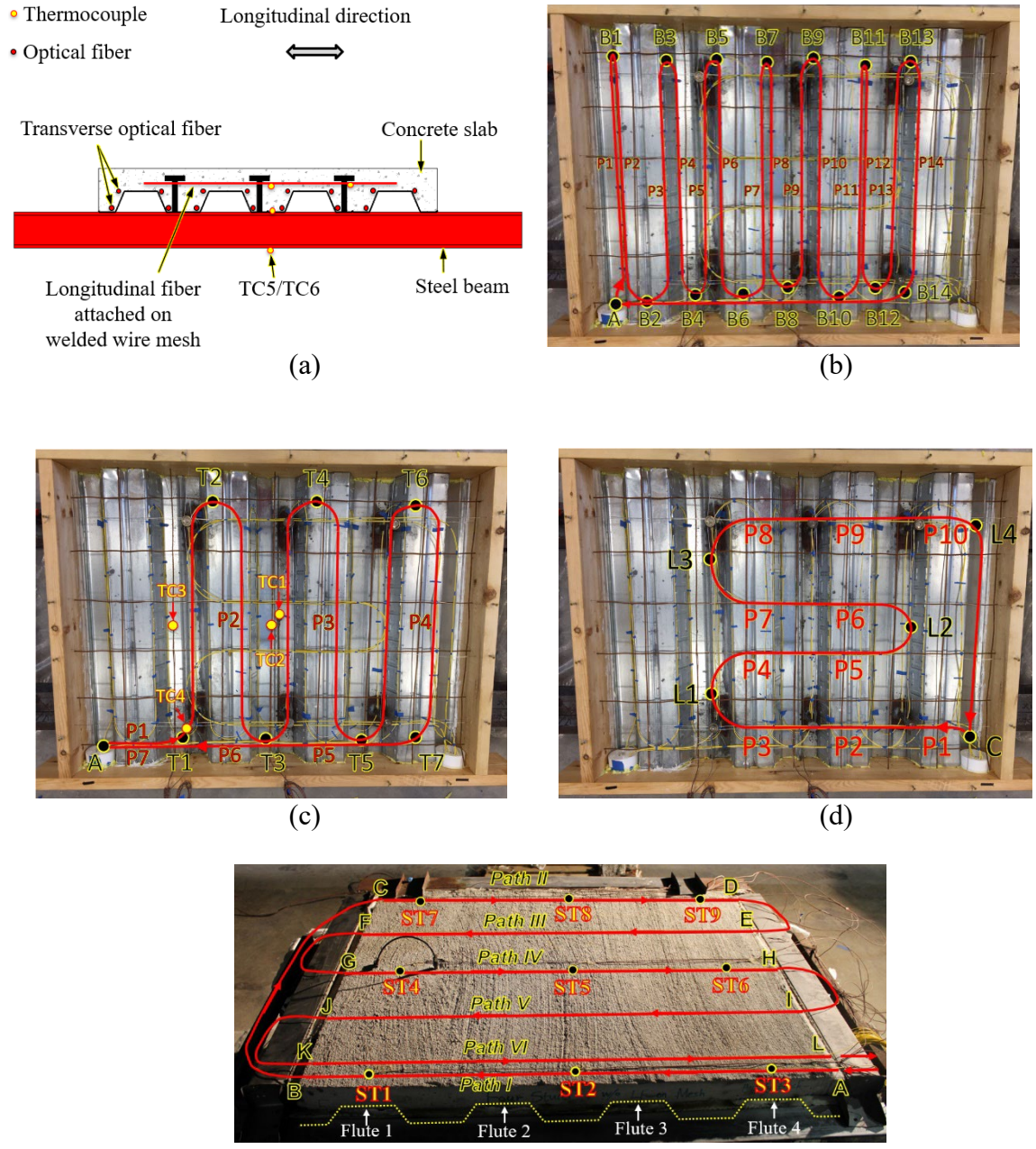

Figure 4.2 Instrumentation layout: (a) elevation view, (b) top view of DFOS-1, (c) top view of DFOS-2, (d) top view of DFOS-3, and (e) top view of DFOS-4

4.3 Test Setup

Fire tests were conducted in the National Fire Research Laboratory at the National Institute of Standards and Technology (NIST). The test setup was not intended to represent a particular structure, but rather to investigate the performance of distributed sensors in a typical steel–concrete composite structure. Figure 4.3 depicts the test setup located under a 6 m × 6 m (plan) exhaust hood. The flame source was a natural gas diffusion burner measuring 530 mm × 530 mm × 200 mm (length × width × height). Natural gas entered the burner near the bottom, filled the burner cavity, and percolated through a gravel layer to distribute the gas. The burners were manually regulated using a needle valve on the gas supply line. A skirt constructed of cold-formed steel framing and cement board lined with thermal ceramic fiber blankets partially enclosed the space above the burner to trap hot gases beneath the specimen. The skirt was open at the bottom, creating the compartment fire depicted in Figure 4.3(a). The heated compartment created by the skirt was approximately 1220 mm × 920 mm × 300 mm (length × width × height). Each beam was simply-supported at a clear-span of 1530 mm on four supports made of stacked concrete masonry units (CMU). The supports were wrapped with 25-mm thick thermal ceramic blankets for thermal protection.

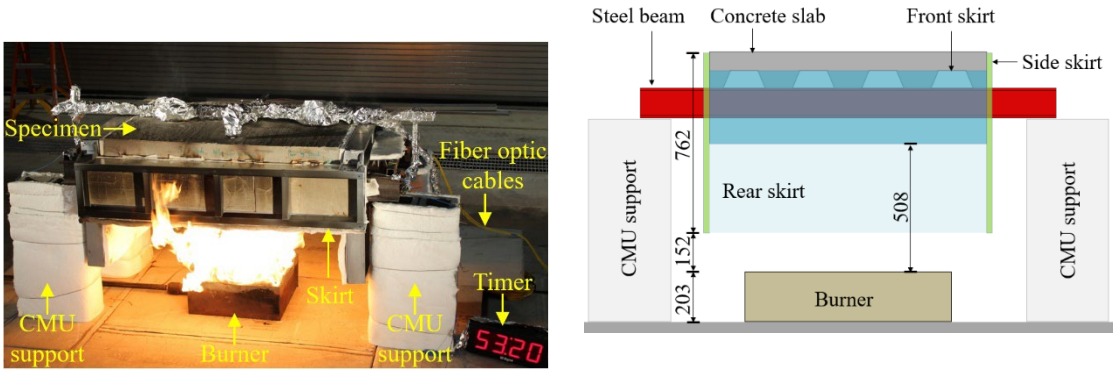

(a) (b)

Figure 4.3 Test setup: (a) photograph, and (b) illustration (units in mm)

4.4 Fire Testing Protocol

All specimens were subjected to a similar fire protocol with a peak heat release rate (HRR) of 200 kW. No mechanical load beyond self-weight was applied. The magnitude of fire was controlled through the burner's calculated heat release rate. Figure 4.4 shows the burner HRR, compartment upper layer gas temperature, and beam temperatures measured from TC5 and TC6 peened into the bottom flange of the steel beams along the centerline. No thermocouple was deployed on the steel beams of specimen CS-1 and only one beam thermocouple was deployed in CS-3 and CS-5.

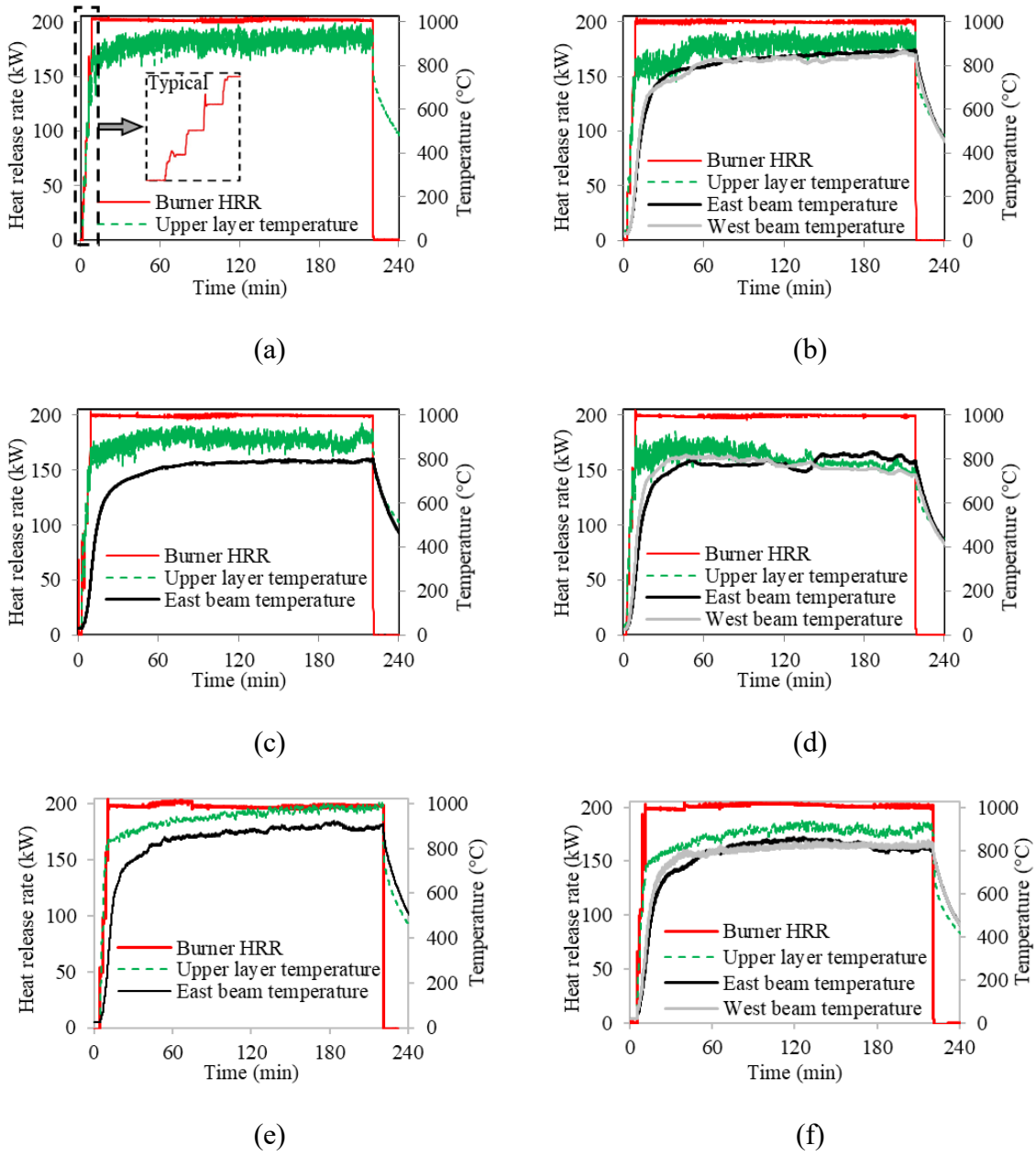

Figure 4.4 Heat release rate and temperature: (a) CS-1, (b) CS-2, (c) CS-3, (d) CS-4, (e) CS-5, and (f) CS–6

The heat release rate was held approximately constant at 50 kW, 100 kW, 150 kW, and 200 kW. Each of the first three levels was maintained for 2 min; the last level (200 kW) was maintained for 210 min, before the fire was extinguished. In total, each specimen was heated for approximately 216 min (3 h 36 min). For specimens CS-1 to CS-3 and CS-6, the upper layer gas

temperature was 897 °C ± 38 °C (mean ± standard deviation) when the heat release rate was 200 kW, as shown in Figure 4.4. During the fire test of specimen CS-4, a burner frame weld failed, skewing the flame, and a small fan was used to redirect the fire beginning at 100 min. The draft caused by the fan changed the fire dynamics and resulted in variations of about 100 °C of air and beam temperatures, as shown in Figure 4.4(d). For specimens CS-5 and CS-6, the compartment height was inadvertently reduced by one CMU block (≈200 mm), which resulted in a slightly higher upper layer temperature and beam temperature as well as possibly a slightly smaller fluctuation of upper layer temperature, as shown in Figure 4.4.

4.5 Results and Discussion

4.5.1 Observations

All the distributed fiber optic sensors survived the installation, concrete casting, and curing process without damage. The two methods of concrete placement, careful hand troweling and direct pouring from a concrete truck chute, did not make a difference on the integrity of the installed sensors.

Shortly after a heat release rate of 200 kW was achieved, popping sounds were heard from the specimen; however, no cracking or spalling was observed on visible surfaces. The sounds were attributed to spalling of the concrete at the interface with the metal decking. After approximately 10 min at 200 kW, separation between the metal decking and concrete was observed, as shown in Figure 4.5(a). After the test, when the specimens had cooled, the metal decking was removed for visual inspection. Figure 4.5(b) shows the bottom of the concrete slab. Some aggregates were visible and believed to result from “micro-spalling” of concrete adjacent to near-surface aggregate, consistent with the popping sounds. The micro-spalling is attributed to moisture in lightweight aggregates creating internal vapor pressure under a fire-induced

temperature increase. Diagonal cracks formed near the mid-span of the concrete slab around 30 min after fire ignition. A crack through the specimen width was visible on the top surface at about 40 min. Additional cracks appeared in the specimen until 200 min. Similar phenomena were observed in the other specimens. It is noted that the timing and sequence of the events are specific to the investigated specimens and fire conditions.

After the fire test, several cylinders measuring 76 mm in diameter were cored from the specimens using a diamond core drill, as depicted in Figure 4.5(b). Cylinders were taken in both the thick (thickness: 159 mm) and thin (thickness: 83 mm) sections of the trapezoidal concrete slab. Channels in the concrete created by the removed welded wire mesh and burnt optical fiber sheathing can be observed. While some polypropylene microfibers could still be observed on the top surface of the concrete, no polypropylene fibers could be found near the bottom surface of the tested specimen. This is an indicator of the temperature variation through the depth of the concrete. The melting point of polypropylene fibers is about 165 °C. In spite of the high relative humidity of the concrete (which relates to the moisture content), no widespread spalling occurred, likely due to the use of polypropylene fibers that melted and provided mechanisms for alleviating internal vapor pressure in the concrete slab (Li et al. 2018).

(a)

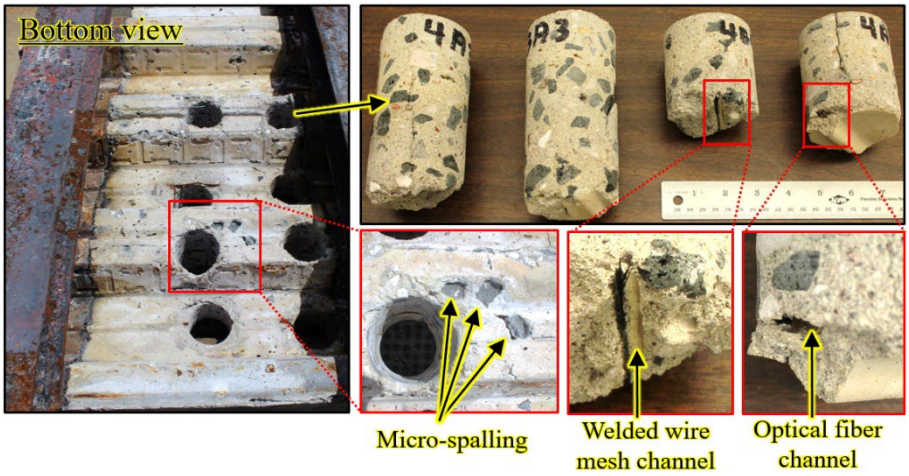

(b)

Figure 4.5 Photograph of CS-1 after fire test: (a) before removal of the steel deck, and (b) after removal of the metal decking at the bottom of the reinforced concrete slab.

4.5.2 DFOS Temperature Measurements

After a constant heat release rate had been achieved, temperature distributions along the length of the distributed sensors DFOS-1, DFOS-2, and DFOS-3 in specimen CS-1 at various

time instants are plotted in Figure 4.6. The times are relative to burner ignition. In each figure, the horizontal axis represents the distance along the distributed sensor, measured from the connection to the data acquisition system. The vertical axis represents the measured temperature, which was obtained from the Brillouin frequency shift measured by the distributed sensor. As expected, temperature increases with time in all three sensors during the heating phase of the experiment. However, the spatial patterns of temperature distribution observed from the three sensors are quite different. The different patterns are primarily due to the different locations of the sensors deployed in the concrete, as depicted in Figure 4.2(b)-(d). The locations of the curved portions of the distributed sensors are marked in Figure 4.6 for reference.

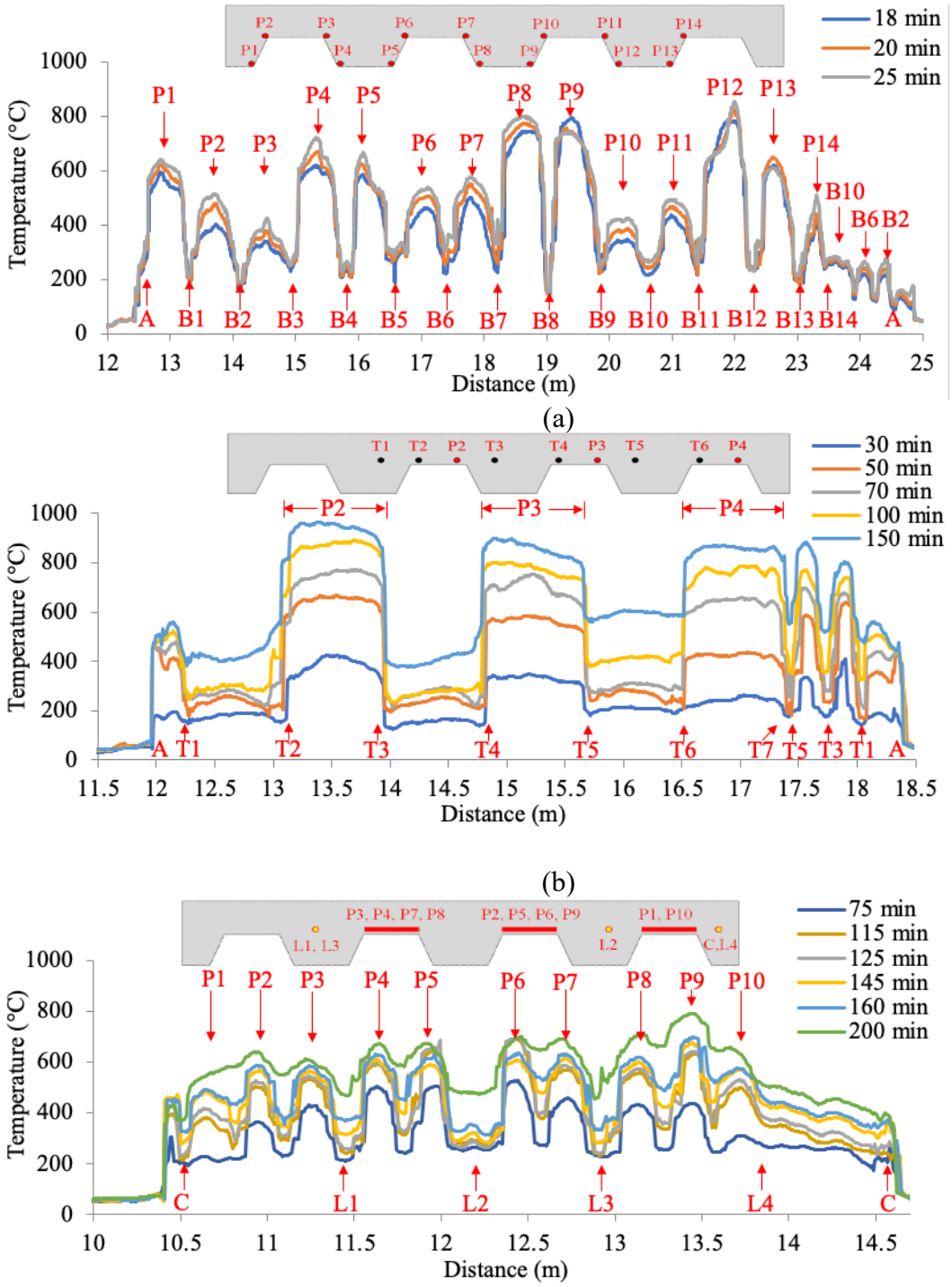

Figure 4.6 Temperature distributions measured from the distributed sensors in specimen CS-1: (a) DFOS-1, (b) DFOS-2, and (c) DFOS-3. The peaks in slab illustration and test results are marked as "Pn", where "n" indicates the location of a peak (see Figure 4.2)

In Figure 4.6(a), the first 14 peaks are marked as P1 to P14 along the centerline of the specimen. DFOS-1 measured the temperature in the bottom of the concrete slab just above the steel deck. The fact that the peaks occurred along the centerline suggests that: (1) the gas temperature and radiative heat flux were lower near the edges of the test setup; (2) there was more heat loss from the specimen to the surrounding environment at its edges; and (3) the steel beams near the edges provided heat sink for the concrete slab. The temperature variation transversely across the specimen is significant: over 600 °C variation for fiber section B8 above a steel beam. This spatial variation has been neglected in thermo-mechanical analysis where it is typically assumed that gas temperature and heat flux below the slab is uniform. P8 and P9 above the burner exhibited the highest temperatures. Overall, the temperatures at P1, P4, P5, P8, P9, P12, and P13 are higher (on the order of 200 °C to 400 °C) than the temperatures at P2, P3, P6, P7, P10, P11, and P14. This comparison suggests that the lower flanges of the concrete slab were subjected to more intense thermal conditions than the higher flanges because they were closer to the burner. The peaks after P14 are marked by the locations of the curved portions of the distributed sensor. For instance, the peak B10, which is the peak after P14 in Figure 4.6(a), corresponds to the portion of the distributed sensor near B10, as seen in Figure 4.2(b). Unlike the previous portion of DFOS-1, the optical fiber ran from B14 to A in a straight line and at a constant height in the concrete slab. The peaks B10, B6, and B2 are therefore associated with the change of the thickness of the concrete slab. Because of the varying thickness of the concrete slab, the distributed sensor at the locations B10, B6, and B2, which are above the upper flanges of the decking, was closer to the metal decking (and thus the hot compartment) than at the locations B12, B8, and B4.

In Figure 4.6(b), the peaks marked by P2 to P4 represent the locations of sensor DFOS-2 parallel to the flute above the thin portions of the deck profile, as depicted in Figure 4.2(c). DFOS-2 measured temperature along the welded wire mesh (the optical fiber was taped to the mesh to maintain its position prior to concrete casting), which was about 8 mm away from the high flute of the metal decking, as illustrated in Figure 4.1(b). Because the welded wire mesh was at a roughly constant height in the concrete slab, the temperature is higher in the optical fiber section above the upper flange of the metal decking (8 mm concrete cover) than in the section above the lower flange of the metal decking (84 mm concrete cover). In each of the peaks P2 to P4, the temperature distribution is approximately constant and the temperature at the centerline is not significantly higher than at the specimen sides, which is different from the observations in Figure 4.6(a). This difference is attributed to three mechanisms. First, the concrete cover serves as a thermal "buffer" that smooths the temperature gradient. Second, the high thermal conductivity of the steel wire mesh (to which the fiber was taped) further reduced any temperature gradient along the fiber. Third, delamination of metal decking decelerated the heat transfer from the metal decking to the concrete slab, reducing the temperature gradient in the concrete slab. Other peaks besides P2 to P4 were due to the geometry of the metal decking. Although a simultaneous comparison of the temperatures in DFOS-1 and DFOS-2 was not possible due to the required data acquisition time for each fiber loop (roughly 5 min), comparing the temperatures between B6 and B7 in DFOS-1 at 25 min and the temperatures between T2 and T3 in DFOS-2 at 30 min (which are roughly comparable in time and horizontal position in the concrete slab), shows the average temperatures are slightly higher in DFOS-1 (374 °C) than in DFOS-2 (369 °C), which is expected based on the concrete cover for each fiber sensor. At 150 min, a temperature up to 960 °C was measured at P2.

The first 10 peaks in Figure 4.6(c) are marked by P1 to P10, which represent the lengths of sensor DFOS-3 in the vicinity of the metal decking, as depicted in Figure 4.2(d). DFOS-3 measured the temperature along the welded wire mesh perpendicular to the direction of the decking flutes. Along the length of DFOS-3, the distance between the fiber optic sensor and the metal decking varied. The temperature is higher in the portions of the sensor closer to the metal decking than in the portions further from the decking. As the fire testing time increases from 160 min to 200 min, the peaks become less prominent. This trend indicates the temperature gradient in the concrete slab decreases over time as the temperature of the entire concrete volume increases.

Figure 4.7 shows the surface temperature distributions measured from DFOS-4 sensors in specimens CS-5 and CS-6, respectively. In each specimen, the distributed sensor measured the temperature distributions along the six paths on the top surface shown in Figure 4.2(e). Within the range of each path, four peaks are identified corresponding to the four upper flutes of the concrete deck (F1 to F4), indicating a higher surface temperature at the thin concrete sections; by comparing the temperatures corresponding to each flute in the same path, it is seen Flute 2 and Flute 3 have higher temperatures than Flute 1 and Flute 4, because the middle of the slab directly above the burner experienced a higher temperature than the two ends of the slab, consistent with the observations from Figure 4.6.

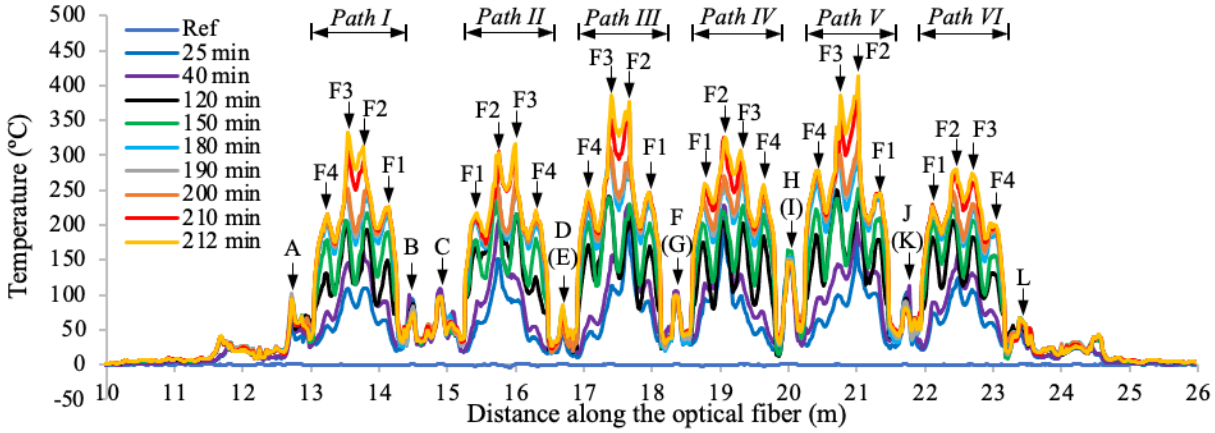

(a)

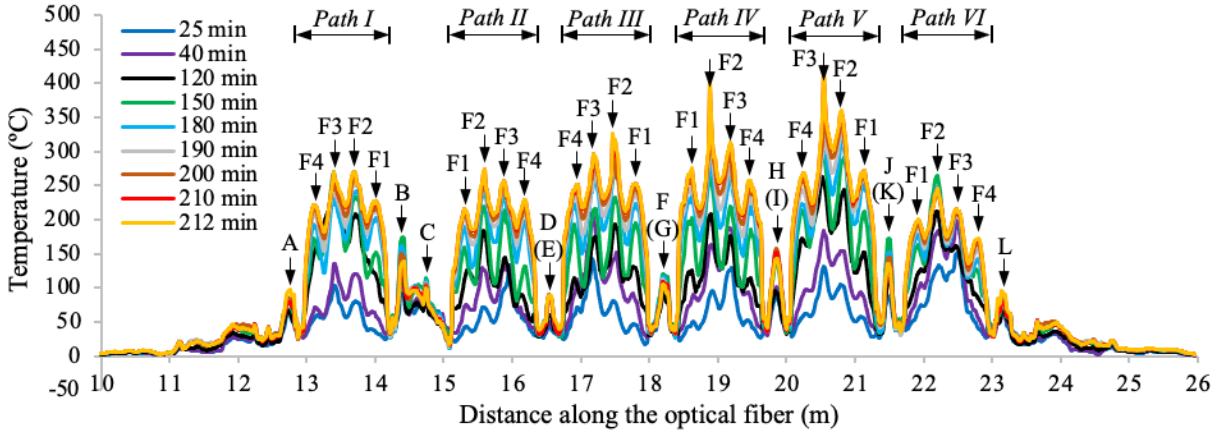

(b)

Figure 4.7 Surface temperature distributions measured from DFOS-4 in: (a) CS-5, and (b) CS-6. "F1" to "F4" stand for Flute 1 to Flute 4 shown in Figure 4.2(e)

4.6 Summary

In this study, temperature distributions were measured using distributed fiber optic sensors installed in steel–concrete composite slab specimens exposed to fire. Compared with traditional point sensors, e.g., thermocouples, this approach provided a significantly higher spatial resolution of temperatures.

This limited set of data suggests that the investigated polymer-sheathed optical fibers survived the concrete casting process in typical building construction. The temperatures measured using the distributed sensors were in reasonable agreement with the results from thermocouples deployed close to the distributed fiber optic sensors. The measured temperature discrepancies between the fiber optic sensors and the thermocouples were attributed to position differences in the specimens. Further study is recommended to verify this. Material temperatures up to 960 °C were measured at the interface between the concrete and the metal deck.

The measured temperatures from a distributed fiber optic sensor indicate highly non-uniform patterns of temperature distribution in each composite slab specimen, which are often neglected in engineering design and analysis. Deploying the distributed fiber optic sensors in large-scale structural fire tests has the potential to improve our understanding of the performance of infrastructure in fires and, thus, fire safety.

Chapter 5 Distributed Fiber Optic Measurement of Temperature in Long-span Composite Floor Beams with Simple Shear Connections Subject to Fires

5.1 Introduction

Structural response to fires has been widely studied using physical experiments and numerical models (Bisby et al. 2013; Franssen et al. 2017). Measured or calculated temperature distributions are often used to evaluate structural response using coupled thermal-mechanical analysis (Kodur et al. 2008; Jeffers et al. 2009) (Jiang et al. 2018). However, it remains cumbersome to measure temperature distributions with high spatial resolution in structural materials such as concrete under fire conditions (Yang et al. 2015). Historically, discrete (point) temperatures have been measured using thermocouples; however, dozens, or even hundreds, of thermocouples must be placed in the concrete formwork prior to casting to get even a coarse indication of the horizontal and through-depth temperature variation in concrete during heating for large structures. This is cost and time intensive. Although infrared cameras provide valuable information about temperature distribution over large areas, they are not suited measurements of temperature variation through the depth of a material and can be susceptible to error caused by changes in surface conditions as well as the presence of flames in the field of view of the camera (Hoehler et al. 2020).

Fiber optic sensors for measuring temperature have seen increased use in structural fire research due to their ability to survive harsh environmental conditions (Bao et al. 2019). For example, fiber Bragg grating (FBG) sensors have been used to measure strain and temperature up to approximately 300 °C when traditional gratings are annealed (erased) (Zhang and Kahrizi 2007). Huang et al. (2013, 2010) used long-period fiber grating (LPFG) sensors to measure strain and temperature up to 700 °C. To extend the temperature range further, regenerated FBG (rFBG)

sensors were used by Rinaudo et al. (2015) to record strain and temperature up to 970 °C. Although grating-based sensors could measure high strain and temperature, they provide measurements only at a single location; i.e. the location of the gratings. More recently, measurements that are distributed along the length of an optical fiber, without the need for a grating, have become feasible due to developments such as Brillouin optical time domain analysis (BOTDA) and Brillouin optical time domain reflectometry (BOTDR). For example, pulse pre-pump BOTDA (PPP-BOTDA) has been developed with spatial resolution of 2 cm over 500 m of fiber length. Using this emerging technology in structural condition monitoring to measure strain distributions and detect cracks at ambient temperature has been explored (Bao et al. 2017a, 2015). PPP-BOTDA technology used for temperature and strain measurement under fire conditions is still limited. Bao et al. (2016a and b) studied and calibrated temperature-dependent strain and temperature sensitivities of PPP-BOTDA sensors and went on to use the sensors for strain and temperature measurements in simply-supported steel beams under fire conditions (Bao et al. 2016c). Additionally, Bao et al. (2017b) studied temperature measurement and damage detection in concrete beams exposed to fire using PPP-BOTDA sensors and the conducted experiments on the deployment of the technique in small (1.2 m × 0.9 m) steel-concrete composite slabs (Bao et al. 2020). Their results showed that one single-mode optical fiber can achieve temperature measurements with accuracy better than 12%, compared to the readings of thermocouples at the same locations.

In this study, distributed fiber optic sensors (DFOS) were deployed for the first time in full-scale steel-concrete composite floor slabs tested under mechanical loading or combined mechanical and fire loading. Under mechanical loading at ambient temperature, the mid-span strains measured in the concrete slab using PPP-BOTDA were compared with those linearly

interpolated or extrapolated from two strain gauges installed in the same cross section. Under combined mechanical loading and fire conditions, the temperatures measured in the concrete slabs using PPP-BOTDA were compared with values linearly interpolated or extrapolated from two thermocouples. Due to undocumented uncertainties in temperature measurement that is required to compensate the discrimination of strain measurements, strain data under the combined mechanical and fire conditions are not reported in this study.

5.2 Experimental Program

5.2.1 Test Specimens

Three 12.8 m long composite floor beams that were part of a larger study of the performance of composite construction in fire (Choe et al. 2020) were instrumented with distributed fiber optic sensors. They were designed with double angle end (shear) connections in accordance with current U.S. codes and standards (ANSI/AISC-360, 2016) (ASCE/SEI 7, 2016). The first beam with no slab end continuity serving as a baseline to the other beams and designated as CB-DA-AMB was tested until failure under mechanical loading at ambient temperature to understand its ultimate strength. Identical to the first beam, the second specimen, designated as CB-DA, was tested to failure under combined mechanical loading and fire. The third beam with slab end continuity, designated as CB-DA-SC, was tested to failure under combined mechanical loading and fire. Design details for the specimens are presented in (Ramesh et al. 2019) (Choe et al. 2019). The magnitude of mechanical loading applied on the second and third beams corresponded to 45% of the ultimate moment capacity of the first beam (Choe et al. 2018). The fire was generated using natural gas burners with a maximum total heat release rate of 4 MW.

Figure 5.1(a) and (b) give the end connection with double angles and slab continuity (using four no. 4 reinforcing bars), and the cross section of the CB-DA-SC specimen, respectively. A 1.83 m wide by 12.8 m long lightweight aggregate concrete slab with polypropylene microfibers was cast on 20-gauge profiled metal decking above a W18×35 steel beam. Headed studs (19 mm shaft diameter) were welded to the steel beam with a spacing of 305 mm. The degree of composite action between the concrete and the beam achieved by the studs was approximately equal to 82% of the ambient yield strength of the steel cross section (W18×35). Welded wire fabric (6×6 W1.4×W1.4) was embedded at 42 mm below the top surface of the concrete to satisfy minimum shrinkage and temperature cracking control requirements in Steel Deck Institute Standard C-2011 (2011). The bottom flange of the steel beam was cut at both ends (Figure 5.1(a)) to accommodate the double angles during construction. For CB-DA-SC, four additional no. 4 steel reinforcing bars were embedded in the negative bending moment region near the end supports and anchored to a hollow steel section to simulate the slab continuity. The steel beam was coated with sprayed fire resistive materials (SFRM) to achieve a 2-hour fire resistance rating along the member and a 3-hour fire rating at the connections.

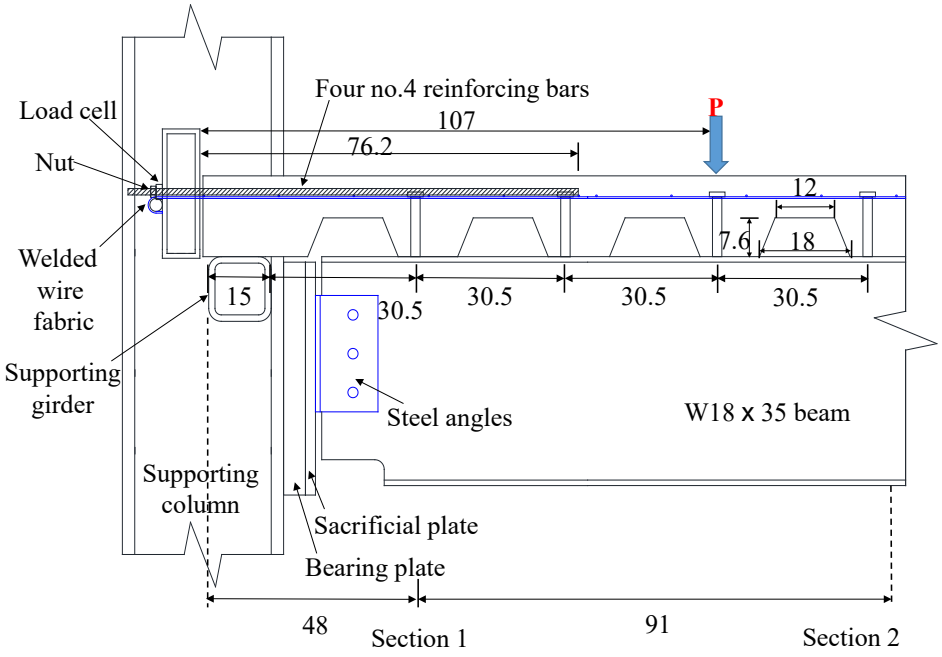

(a)

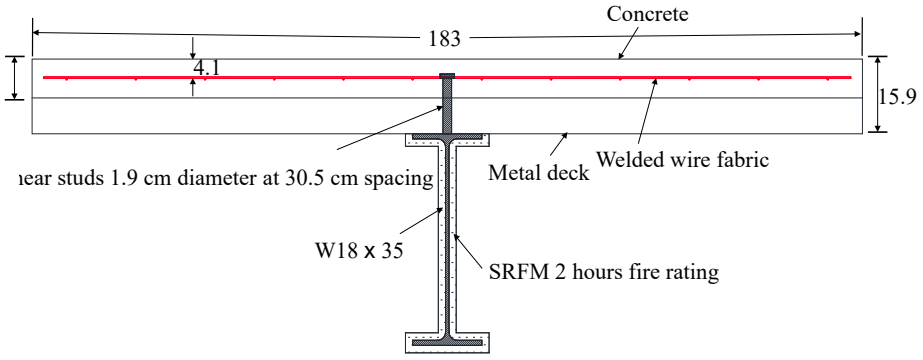

(b)

Figure 5.1 Scale drawings of (a) the specimen-to-column connection and (b) the transverse cross-section of specimens (Units: cm)

5.2.2 Material Properties

A full description of the specimen material properties is available in (Choe et al. 2020). Select properties relevant to the distributed fiber optic sensors are provided here. All material properties were determined in accordance with the relevant ASTM standards (A325, A36, A185,

A29, A615, A992, C143, C39, and C642). Polypropylene microfiber reinforced lightweight aggregate concrete with a water-to-binder ratio of 0.46 was used for the test specimens. High-range water reducer was added to achieve a design slump of 216 mm and limit the required mechanical vibration of the concrete. This was intended to prevent breakage of the distributed optical fiber sensors during casting. The polypropylene microfibers (25 mm long and 40 μm in diameter at a dosage of 2.37 kg/m^3) were used to reduce the likelihood of spalling of the concrete under fire conditions (Li et al. 2017). The mean 28-day concrete cylinder compressive strength was 45.4 MPa. After curing for 6 months, internal relative humidity in the concrete dropped to about 80%. The fire experiments were conducted about 12 months after the concrete placement. For the W18×35 beams, the measured yield and ultimate tensile strengths were 360 MPa and 470 MPa, respectively. The modulus of elasticity of the steel beams was 203 GPa. The measured ultimate strength for bolts, shear studs, and welded wire fabrics was 960 MPa, 510 MPa, and 760 MPa, respectively.

5.3 Test Setup and Instrumentation

The test setup is shown in Figure 5.2. The test specimen, for which the soffit of the slab was elevated 3.8 m above the laboratory floor, was attached to longitudinally braced W12x106 steel columns at the west and east ends. Six equally distributed point loads were applied to the specimen along its centerline using three pairs of servo-hydraulically controlled actuators attached to the ends of loading beams coupled with triangular loading trusses. To confine the fire below the specimen, enclosure walls were constructed below the specimen using cold-formed steel framing and sheet steel. The fire-exposed wall surfaces were protected with two layers of 25 mm thick ceramic fiber blankets. Three natural gas diffusion burners with servo-controlled gas mass flow were arranged along the center of the compartment floor and were used to heat the

specimen. This setup replicated a 1.83 m wide strip of a building around the beam-column centerline for which a realistic fire and design gravity load could be simultaneously applied at full-scale.

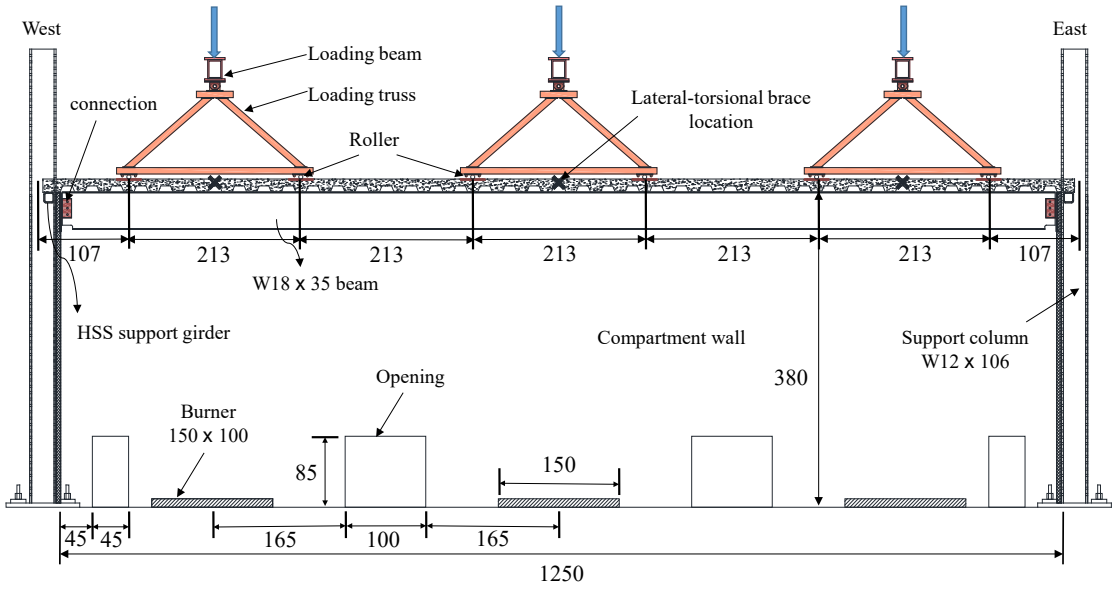

Figure 5.2 Scale drawing of longitudinal section of the experimental setup (Units: cm)

Three strain distributed fiber optic sensors (L-DFOS) were placed longitudinally along the centerline of the beam at approximately 32 mm, 51 mm, and 70 mm below the top surface of the concrete as shown in Figure 5.3(a). Two temperature fiber optic cables were co-located with the top and bottom strain sensors. The longitudinal sensors were taped to thin wires spanning from end-to-end in the slab so that they could maintain their position during concrete casting. As shown in the caption of Figure 5.3(a), all five L-DFOS were collected and turned by 90° to an exit point for data acquisition during tests. Additionally, two transverse distributed fiber optic sensors (T-DFOS) were deployed in a zig-zag pattern on the weld wire fabric (reinforcement) to measure the temperature distribution in the concrete slab approximately 41 mm from its top

surface (Figure 5.3(b)). Since the top L-DFOS was placed prior to the installation of the T-DFOS, the transverse fibers were raised for about 10 mm in elevation near the centerline of the specimen as detailed in the insert of Figure 5.3(b). Several of the sensors were spliced together in a series outside the concrete so their data could be acquired simultaneously on a single analyzer. The strain and temperature distributed fiber optic sensors have a 95% confidence interval of $\pm$ 1.63% and $\pm$ 3.66%, respectively, based on the coefficient of variation of nine adjacent measurement points.

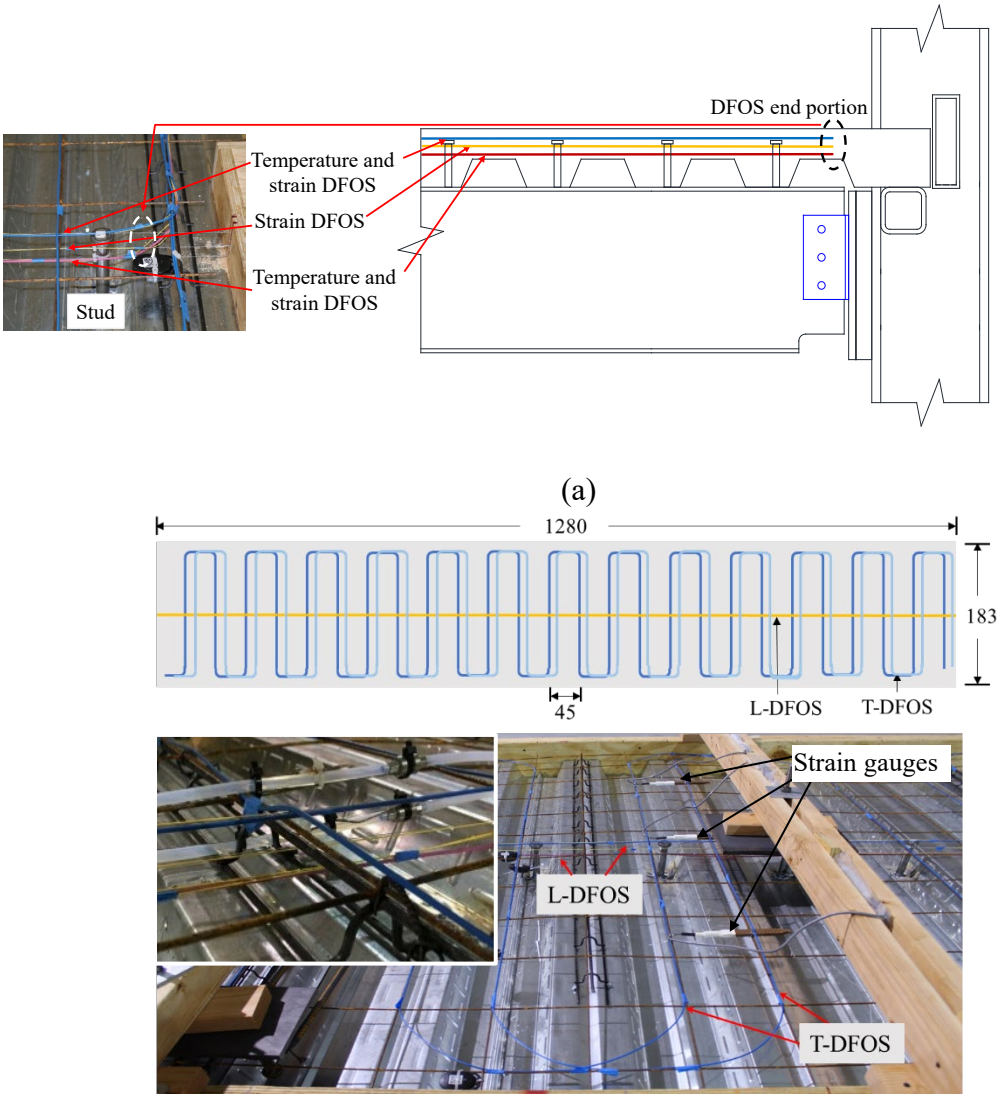

Figure 5.3 Specimen instrumentation: (a) longitudinal distributed fiber optic sensors (L-DFOS) for temperature and strain and (b) transverse distributed fiber optic sensors (T-DFOS) and strain gauges (Units: cm)

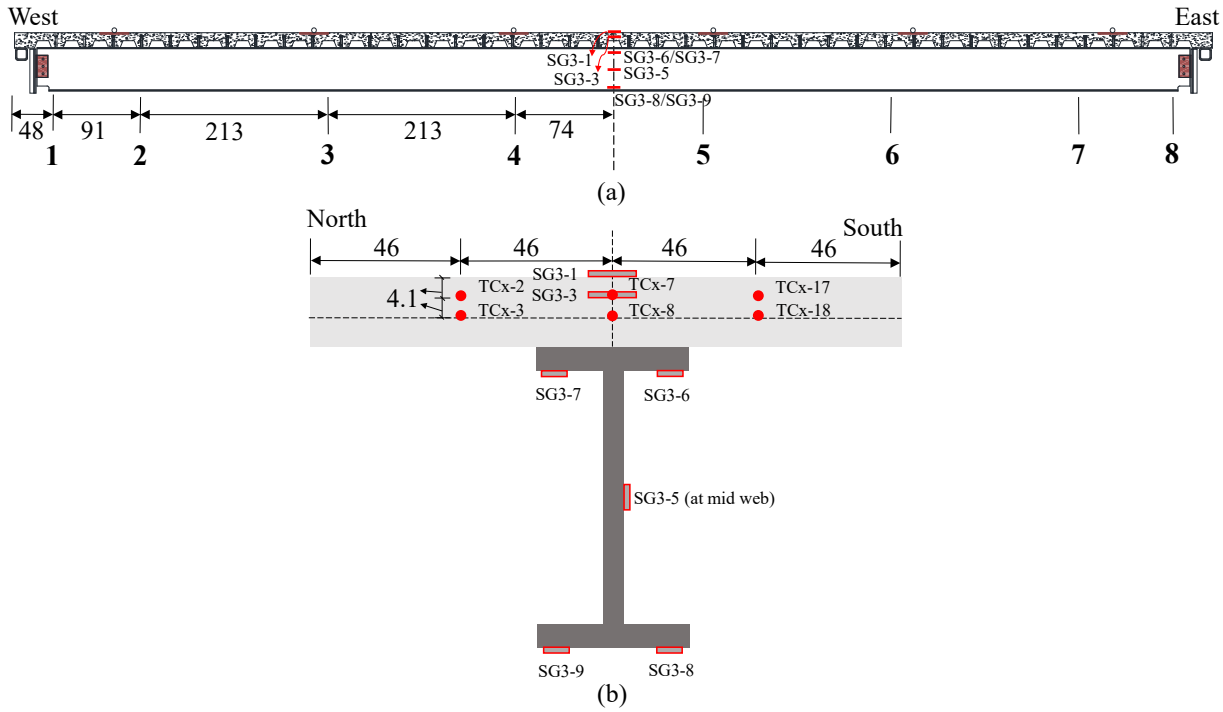

Figure 5.4 Locations and labels of Type K thermocouples (TC) mounted on each specimen: (a) cross section numbers (x=1 through 8) and (b) TC designations at each cross section and strain gauges (SG) at mid-span cross section (Units: cm)

To validate the spatially-distributed temperature measurements from the distributed fiber optic sensors, six glass-sheathed 24-gauge Type K thermocouples (TC) were deployed on the welded wire fabric and top of the metal decking at each of the eight sections (x = 1 through 8) as shown in Figure 5.4. At each section, two thermocouples (TCx-7 and TCx-8) were installed right above the steel beam in the centerline, two (TCx-2 and TCx-3) were located at 46 cm north of the beam centerline and two (TCx-17 and TCx-18) at 46 cm south of the beam centerline. At the mid-span section of the CB-DA-AMB specimen, two strain gauges were deployed in the concrete slab: one on the top surface and the other at 4.1 cm below in the concrete. Additional strain gauges were installed at the top and bottom flanges as well as the mid-height web of the steel beam.

The location where each optical fiber run entered and exited the concrete as detected by the PPP-BOTDA analyzer was determined immediately prior to the fire testing. This was done by placing an ice cube on points of interest of the fiber which provided a measurable localized temperature decrease. The position of the fibers inside the concrete had been mapped prior to concrete casting.

5.4 Test Protocols

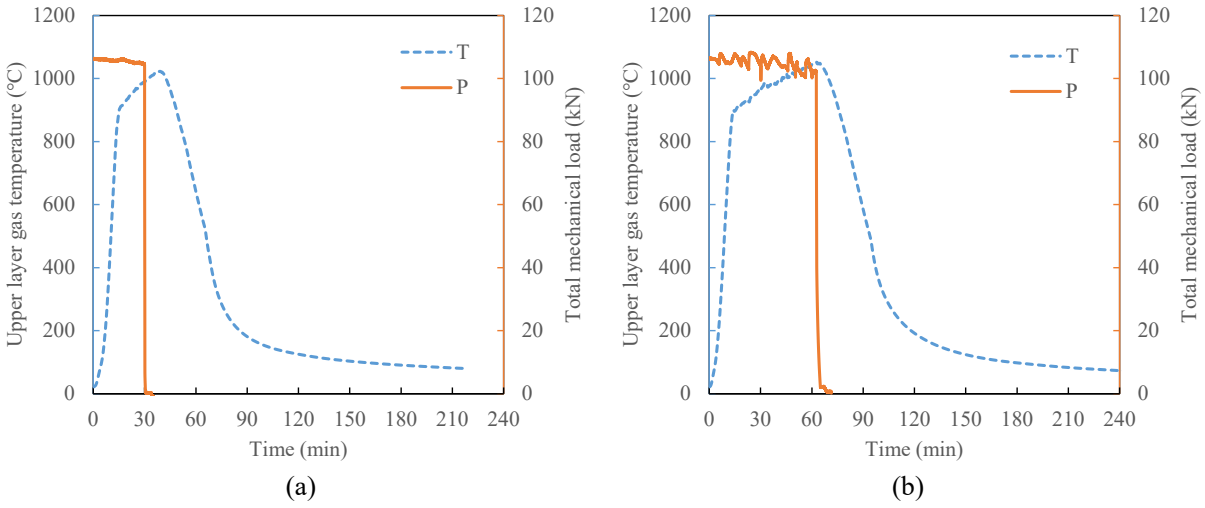

Figure 5.5 Gas temperature (T) measured 81 cm below concrete slab and total applied mechanical load (P) for (a) CB-DA specimen and (b) CB-DA-SC specimen

The experimental protocol used for CB-DA and CB-DA-SC specimens was as follows: (1) a total mechanical load of 106 kN (17.7 kN/point load or 45 % of the ultimate moment) was applied and held constant at ambient temperature, (2) the heat release rate in the compartment under the beam was increased to 4 MW over a period of 15 min and held constant, and (3) a cooling phase was initiated by linearly decreasing the heat release rate over 30 min. The applied total mechanical loading and compartment upper layer gas temperature histories for the

specimens instrumented with distributed fiber optic sensors are shown in Figure 5.5. Note that the applied point load (17.7 kN) is slightly higher than 0.25 Pmax = 15.75 kN.

5.5 Results and Discussion

5.5.1 Temperature Distribution from Longitudinal DFOS in Fire Conditions

Figure 5.6 compares concrete temperatures measured at different times from the longitudinal DFOS and thermocouples deployed along the centerline of the CB-DA specimen that was tested under simultaneous mechanical and fire loads. The fiber optic temperature sensors were located 32 mm (Top) and 70 mm (Bottom) below the top surface of the concrete slab. Their closest thermocouples were positioned at 41 mm and 82 mm from the top surface of the slab. Therefore, the thermocouple temperatures were linearly interpolated or extrapolated to obtain the temperatures at the locations of the fiber optic sensors for comparison.

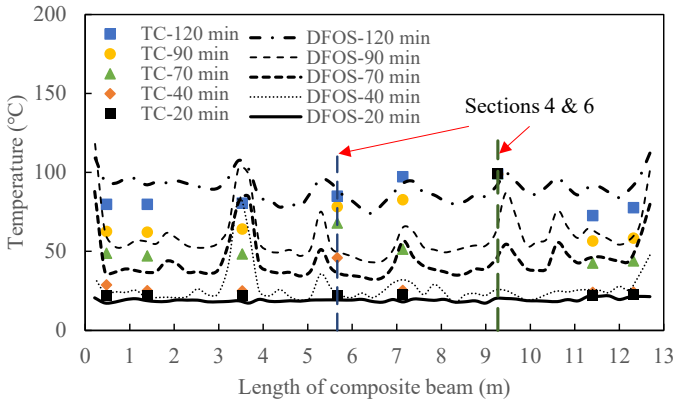

(a)

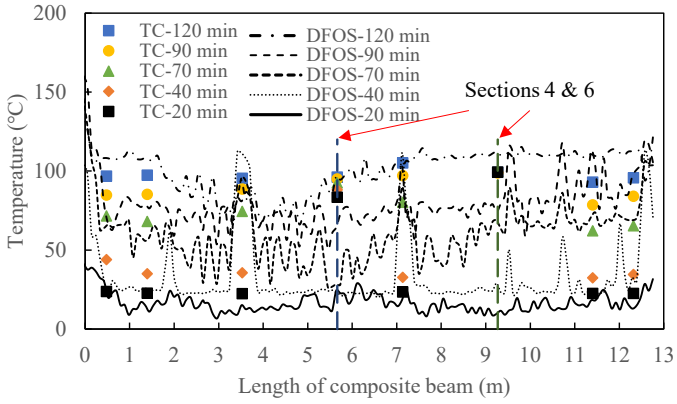

(b)

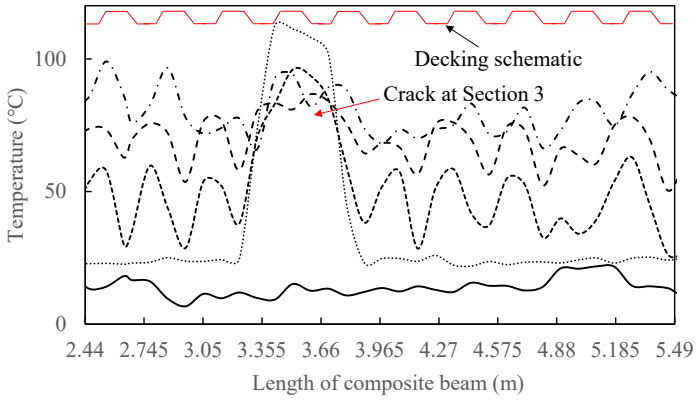

(c)

Figure 5.6 Concrete slab temperatures measured from thermocouple (TC) and distributed fiber optic sensors (DFOS) in CB-DA specimen at various times after fire ignition: (a) 32 mm and (b) 70 mm below the top surface of the slab, and (c) 70 mm below the top surface of the slab (between 2.44 m and 5.49 m) in (b)

The thermocouple temperatures in Figure 5.6(a, b) at a given time follow a roughly horizontal line along the length of the specimen; except at Section 4 (Bottom) and Section 6 (Top and Bottom) where temperatures jump suddenly to 100 °C 20 min into the test. While the amplitude of 100 °C at Sections 4 and 6 is likely caused by water vaporization, the rise time is clearly erroneous – possibly caused by multiple unintended junctions in the lead wires, and these data are disregarded in the subsequent analysis.

The DFOS also exhibits an overall horizontal temperature distribution along the specimen, particularly the top temperature sensor; however, the curves show prominent local temperature peaks. The large, non-periodic singular peaks in the DFOS temperature are likely associated with the formation of cracks in the concrete. There are also smaller amplitude periodic variations visible in the DFOS readings. Due to the trapezoidal shape of the metal decking, the concrete cover to the bottom optical fiber from the fire varies from 13 cm to 89 cm over a length of 30.5 cm (refer to Figure 5.1(a)). This results in periodic local temperature fluctuation along the length of the composite beam as can be seen most clearly in the data extracted from Figure 5.6(b) between 2.44 m and 5.49 m and is shown in Figure 5.6(c). The local maxima represent the locations of the thinner concrete cover (13 cm) to the heated surface of the slab; however, this behavior is complicated by the presence of the cracks in the concrete which cause prominent singular temperature variations. This amplitude fluctuation at 30.5 cm spacing is most pronounced at 70 min, i.e., during the controlled cooling phase of a fire, and then gradually disappears.

Figure 5.7 shows the test data for the CB-DA-SC specimen. Like the CB-DA specimen, the unique information provided by the DFOS not apparent in the thermocouple data is the local spatial variation of temperature. A prominent example of this can be seen between Section 3 and

Section 6. There are indications of significant cracks formed at the bottom of the concrete slab near Sections 3 and 4, and at the top of the slab near Sections 5 and 6. Once the concrete has been fully desiccated at the sensor location after 70 min of burning, the local temperature variation at the cracks becomes less prominent than those seen in the lower fiber denoted in Figure 5.7(b). Note that minor cracks likely occur between Section 5 and 8 close to the lower fiber. As with specimen CB-DA, low-amplitude periodic temperature variations are visible along the optical fiber between 7.67 m and 10.72 m resulting from the varying concrete cover thickness to the heat source (Figure 5.7(c)).

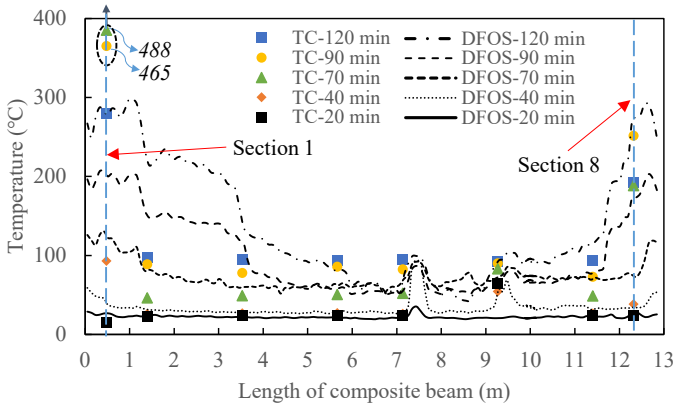

(a)

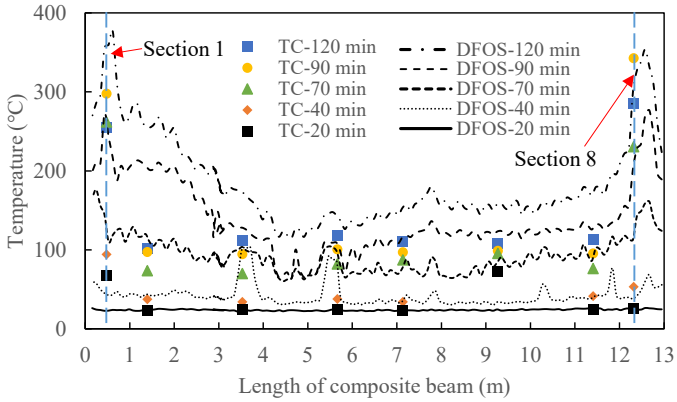

(b)

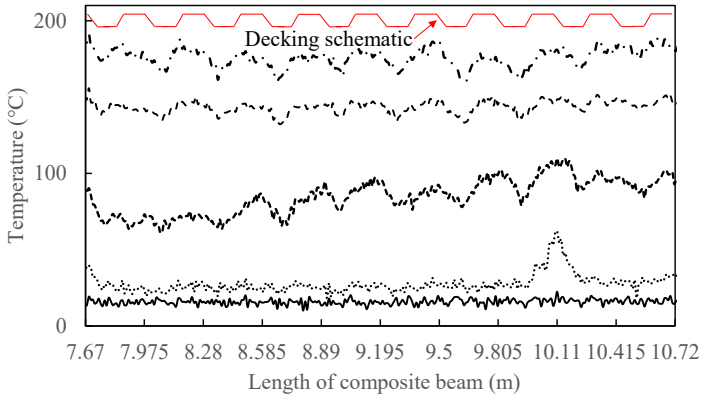

(c)

Figure 5.7 Concrete slab temperatures measured from TC and DFOS in CB-DA-SC specimen at various times after fire ignition: (a) 32 mm, (b) 70 mm below the top surface, and (c) 70 mm below the top surface of the slab (between 7.67 m and 10.72 m) in (b)

Unlike the CB-DA specimen, both the thermocouple data and the DFOS data of the CB-DA-SC specimen indicate a temperature rise near the ends of the slab compared to the middle of the slab. This is due to the pronounced cracking in these portions of the slab, which provided additional paths for moisture transport out of the concrete. For the CB-DA specimen, the end temperature rise is not prominent because the heating of the slab was stopped 40 min after burner ignition before the moisture had been driven out of the concrete at the sensor locations. For specimen CB-DA-SC, the end continuity provided by four reinforcing bars and a longer heating time led to a larger bending deformation of the specimen and therefore multiple large cracks were observed at the top side of the concrete slab. During the experiment the concrete slab above the west angle connection cracked at 43 min, released black smoke on top of concrete at 48 min, and flames were visible at 54 min. The concrete slab near the east support cracked at 50 min, released black smoke at 52 min, and flames were visible at 60 min. Thus, the thermocouple readings at the end portion of the concrete slab are indicative of flame/hot air temperature through penetrated cracks, resulting in a temperature difference of over 200 °C between two closely spaced thermocouples (e.g., TCx-7 and TCx-8) at 65 min. As a result, thermocouple data at Sections 1 and 8 are not used for comparison with the DFOS data in the following analysis.

The combined effect of the opening of metal deck seams and multiple penetrated concrete cracks caused the rise in temperature at the end. The heat radiation through the metal decking and heat convection through the seam opening and concrete cracks are combined to create the complicated mechanical and thermal field in the CB-DA-SC specimen. While the thermocouple measurement indicates the end of the slab cooling between 90 min and 120 min due to moisture evaporation, the DFOS indicates a continued increase in temperatures. This inconsistency is likely attributed to the unintended strain induced along the distributed

temperature sensor by multiple cracks (both top and bottom of the concreate slab) in addition to other factors discussed for the CB-DA specimen.

5.6 Summary

This study applied pulse pre-pumped Brillouin optical time domain analysis along a single-mode optic fiber for strain and temperature measurements in large-scale concrete composite structures. For temperature measurements under simultaneous mechanical loading and fire, the effectiveness of distributed fiber optic sensors was verified against thermocouples. Unlike thermocouples, unique peaks relevant to the concrete cracks and regionally periodic temperature variation due to the varying slab thickness can be captured by the distributed sensors under high temperatures. From longitudinal distributed fiber optic sensors, the measured temperature increases with time from ignition as observed from co-located thermocouples.

Chapter 6 Conclusions

In the present study, the experiments were carried out to investigate the feasibility of strain and temperature measurements using distributed fiber optic sensors under high temperatures (or fire condition) in small-scale and large-scale specimens.

Strain inside the cement mortar after exposure to high temperatures was measured by pulse pre-pumped Brillouin optical time domain analysis (PPP-BOTDA) based on fiber optic sensors. PPP-BOTDA measured strain was compared with the results obtained from strain gauges. The comparison indicates the strain transfer from concrete to the optical fiber can be achieved after exposure to high temperatures.

In small-scale steel–concrete composite slab specimens exposed to fire, temperature distributions were measured using distributed fiber optic sensors. Compared with traditional point sensors, e.g., thermocouples, this approach provided a significantly higher spatial resolution of temperatures. This limited set of data suggests that the investigated polymer-sheathed optical fibers survived during the concrete casting process in typical building construction. The temperatures measured using the distributed sensors were in reasonable agreement with the results from thermocouples deployed close to the distributed fiber optic sensors. The measured temperatures from a distributed fiber optic sensor indicate highly non-uniform patterns of temperature distribution in each composite slab specimen, which are often neglected in engineering design and analysis.

Also, PPP-BOTDA along a single-mode optic fiber for strain and temperature measurements was applied in large-scale concrete composite structures. For temperature measurements under simultaneous mechanical loading and fire, the effectiveness of distributed fiber optic sensors was verified against thermocouples. Unlike thermocouples, unique peaks

relevant to the concrete cracks and regionally periodic temperature variation due to the varying slab thickness can be captured by the distributed sensors under high temperatures. Also, from longitudinal distributed fiber optic sensors, the measured temperature increases with time from ignition as observed from co-located thermocouples.

References

AASHTO T 132–87. Standard method of test for tensile strength of hydraulic cement mortars. American Association of State and Highway Transportation Officials; 2018.

ASTM A325-14. Standard Specification for Structural Bolts, Steel, Heat Treated, 105 ksi Minimum Tensile Strength. (2015) 1–8. American Society of Testing and Materials, West Conshohocken, PA.

ASTM A36/A36M-05. Standard Specification for Carbon Structural Steel, Standards. American Society of Testing and Materials, West Conshohocken, PA.

ASTM International. A108–Standard Specification for Steel Bar, Carbon and Alloy, Cold-Finished. American Society for Testing Material: West Conshohocken, PA.

ASTM A185/A185M-07. Standard Specification for Steel Welded Wire Reinforcement Plain Concrete. American Society for Testing Material: West Conshohocken, PA.

ASTM A29/A29M. Standard Specification for Steel Bars, Carbon and Alloy, Hot-Wrought, Changes. American Society for Testing and Materials, West Conshohocken, PA.

ASTM A615. Standard Specification for Deformed and Plain Billet-Steel Carbon Steel Bars, American Society of Testing and Materials, West Conshohocken, PA.

ASTM International. A611–Standard Specification for Structural Steel (SS), Sheet, Carbon, Cold-Rolled. American Society for Testing Material: West Conshohocken, PA.

ASTM A992/A992M-11. Standard Specification for Structural Steel Shapes, American Society of Testing and Materials, West Conshohocken, PA.

ASTM C143/C143M. Standard Test Method for Slump of Hydraulic-Cement Concrete. American Society of Testing and Materials, West Conshohocken, PA.

ASTM C39/C39M. Standard Test Method for Compressive Strength of Cylindrical Concrete Specimens. American Society of Testing and Materials, West Conshohocken, PA.

ASTM C642. Standard Test Method for Density, Absorption, and Voids in Hardened Concrete. American Society of Testing and Materials, West Conshohocken, PA.

ANSI/AISC-360 (2016). Specification for Structural Steel Buildings. American Institute of Steel Construction, Chicago, Illinois.

ASCE/SEI 7 (2016). Minimum Design Loads for Buildings and Other Structures. American Society of Civil Engineers, Reston, Virginia.

Bao, Y., Valipour, M., Meng, W., Khayat, K.H., Chen, G. (2017a). "Distributed fiber optic sensor-enhanced detection and prediction of shrinkage-induced delamination of ultra-high-performance concrete overlay." Smart Mater. Struct., 26, 085009.

Bao, Y., Meng, W., Chen, Y., Chen, G., Khayat, K.H. (2015). "Measuring mortar shrinkage and cracking by pulse pre-pump Brillouin optical time domain analysis with a single optical fiber." Mater. Lett. 145, 344–346.

Bao, Y., Chen, G. (2016a). "Temperature-dependent strain and temperature sensitivities of fused silica single mode fiber sensors with pulse pre-pump Brillouin optical time domain analysis." Meas. Sci. Tech. 27.

Bao, Y., Chen G. (2016b). "High-temperature measurement with Brillouin optical time domain analysis of an annealed fused-silica single-mode fiber." Opt. Lett. 41, 3177.

Bao, Y., Chen, Y., Hoehler, M.S., Smith, C.M., Bundy, M., Chen, G. (2016c). "Experimental analysis of steel beams subjected to fire enhanced by Brillouin scattering-based fiber optic sensor data." J. Struct. Eng. 143, 04016143.

Bao, Y.; Chen, Y.; Hoehler, M.S.; Smith, C.M.; Bundy, M.; Chen, G. (2016d) Temperature and Strain Measurements with Fiber Optic Sensors for Steel Beams Subjected to Fire. In Proceedings of the 9th International Conference on Structures in Fire, Princeton, NJ, USA, 8–10 June 2016.

Bao, Y.; Chen, G. (2015). Fully-distributed fiber optic sensor for strain measurement at high temperature. In Proceedings of the Tenth International Workshop on Structural Health Monitoring, Stanford, United States, 1–3 September 2015; Chang, F.K., Kopsaftopoulos, F., Eds.; DEStech Publications Inc.: Lancaster, PA, USA.

Bao, Y., Hoehler, M., Smith, C.M., Chen, G. (2017b). "Temperature measurement and damage detection in concrete beams exposed to fire using PPP-BOTDA based fiber optic sensors." Smart Mater. & Struct. 26, 105034.

Bao, Y., Hoehler, M.S., Smith, C.M., Bundy, M., and Chen, G. (2020). "Measuring three-dimensional temperature distributions in steel-concrete composite slabs subjected to fire using distributed fiber optic sensors." Sensors, 20, 5518.

Bao, Y., Huang, Y., Hoehler, M.S., and Chen G. (2019). "Review of fiber optic sensors for structural fire engineering." Sensors, 19 (877).

Bao, Y. Novel Applications of Pulse Pre-Pump Brillouin Optical Time Domain Analysis for Behavior Evaluation of Structures under Thermal and Mechanical Loading. Ph.D. Thesis, Missouri University of Science and Technology, Rolla, MO, USA, 2017.

Bertola, V.; Cafaro, E. (2009). Deterministic–Stochastic approach to compartment fire modelling. P. Roy. Soc. A-Math. Phy. 465, 1029–1041

Bisby, L., Gales, J., Maluk, C. (2013). “A contemporary review of large-scale non-standard structural fire testing.” Fire Sci. Rev, 2(1).

Bundy, M.F.; Hamins, A.P.; Johnsson, E.L.; Kim, S.C.; Ko, G.; Lenhert, D.B. (2007). Measurements of Heat and Combustion Products in Reduced-Scale Ventilation-Limited Compartment Fires; NIST Technical Note; publisher: National Institute of Standards and Technology, Gaithersburg, United States, volume 1483.

Bryant, R.; Bundy, M. (2019). The NIST 20 MW Calorimetry Measurement System for Large-Fire Research; Technical Note; publisher: National Institute of Standards and Technology, Gaithersburg, United States, volume 2077.

Choe, L., Ramesh, S., Grosshandler, W., Hoehler, M., Seif, M., Gross, J., Bundy, M. (2020) “Behavior and limit states of long-span composite floor beams with simple shear connections subject to compartment fires : experimental evaluation.” ASCE J. Struct. Eng. 146, 1–14.

Choe, L., Ramesh, S., Hoehler, M.S., Seif, M.S., Bundy, M., Reilly, J., Glisic, B. (2019) Compartment Fire Experiments on Long-Span Composite-Beams with Simple Shear Connections Part 2: Test Results. NIST Technical Note 2055, Gaithersburg, MD.

Choe, L., Ramesh, S., Hoehler, M., Gross, J. (2018). “Experimental study on long-span composite floor beams subject to fire: baseline data at ambient temperature.” Structures Congress, 133–144.

Franssen, J.M., Gernay, T. (2017). “Modeling structures in fire with SAFIR®: Theoretical background and capabilities.” J. Struct. Fire Eng. 8, 300–323.

Garlock, M., Paya-Zaforteza, I., Kodur, V., and Gu, L. (2012). “Fire hazard in bridges: Review, assessment and repair strategies.” Eng. Struct., 35, 89–98.

Hoehler, M.S. (2020) “On the development of a transparent enclosure for 360° video cameras to observe severe fires in situ.” Fire Safety J, 103024.

Hoehler, M.S.; Smith, C.M. (2016). Influence of Fire on the Lateral Load Capacity of Steel-Sheathed Cold-Formed Steel Shear Walls-Report of Test. US Department of Commerce, National Institute of Standards and Technology.

Huang, Y., Fang, X., Bevans, W.J., Zhou, Z., Xiao, H., Chen, G. (2013). “Large-strain optical fiber sensing and real-time FEM updating of steel structures under the high temperature effect.” Smart Mater. Struct, 22.

Huang, Y., Zhou, Z., Zhang, Y., Chen, G., Xiao, H. (2010). “A temperature self-compensated LPFG sensor for large strain measurements at high temperature.” IEEE Trans. Instr. Meas, 59, 2997–3004.

Inaudi D, Glisic B. Distributed Fiber Optic Strain and Temperature Sensing for Structural Health Monitoring. In The Third Int'l Conference on Bridge Maintenance, Safety and Management, IABMAS'06; 2006; Porto, Portugal

Jeffers, A.E., Sotelino, E.D. (2009). "Fiber heat transfer element for modeling the thermal response of structures in fire." J. Struct. Eng, 135, 1191–1200.

Jiang, L., Usmani, A. (2018). "Towards scenario fires – modelling structural response to fire using an integrated computational tool." Adv. Struct. Eng, 21, 2056–2067.

Kodur, V.K.R., Dwaikat, M. (2008). "A numerical model for predicting the fire resistance of reinforced concrete beams." Cem. Con. Compos, 30, 431–443.

Kodur, V.; Dwaikat, M.; Fike, R. (2010). "High-temperature properties of steel for fire resistance modeling of structures." J. Mater. Civ. Eng. 22, 423–434.

Lamont, S.; Gillie, M.; Usmani, A.S. (2007). Composite steel-framed structures in fire with protected and unprotected edge beams. J. Constr. Steel Res. 63, 1138–1150.

Li, G.Q., Zhang, N., Jiang, J. (2017). "Experimental investigation on thermal and mechanical behaviour of composite floors exposed to standard fire." Fire Safety J. 89, 63–76.

Li, X.; Bao, Y.; Wu, L.; Yan, Q.; Ma, H.; Chen, G. Zhang, H. (2017) Thermal and mechanical properties of high-performance fiber-reinforced cementitious composites after exposure to high temperatures. Constr. Build. Mater. 157, 829–838.

Li, X.; Bao, Y.; Xue, N.; Chen, G. (2017). Bond strength of steel bars embedded in high-performance fiber-reinforced cementitious composite before and after exposure to elevated temperatures. Fire Safety J. 92, 98–106.

Li, X.; Xu, Z.; Bao, Y.; Cong, Z. (2019). Post-fire seismic behavior of two-bay two-story frames with high-performance fiber-reinforced cementitious composite joints. Eng. Struct. 183, 150–159.

Li, X.; Xu, H.; Meng, W.; Bao, Y. (2018). Tri-axial compressive properties of high-performance fiber-reinforced cementitious composites after exposure to high temperatures. Constr. Build. Mater. 190, 939–947.

Liu, H. *et al.* (2016) 'Strain measurement at high temperature environment based on Fabry-Perot interferometer cascaded fiber regeneration grating', Sensors and Actuators, A: Physical. Elsevier B.V., 248, pp. 199–205.

Lonnermark, A.; Hedekvist, P.O.; Ingason, H. (2008). Gas temperature measurements using fibre Bragg grating during fire experiments in a tunnel. Fire Safety J. 43, 119–126.

Maluk, C.; Bisby, L.; Terrasi, G.P. (2017). Effects of polypropylene fibre type and dose on the propensity for heat-induced concrete spalling. Eng. Struct. 141, 584–595.

McGrattan, K.; McDermott, R.; Mell, W.; Forney, G.; Floyd, J.; Hostikka, S.; Matala, A. Modeling the Burning of Complicated Objects Using Lagrangian Particles. In Proceedings of the Twelfth International Interflam Conference, Nottingham, UK, 5-7 July 2010 ; Interscience Communications: London, UK, pp. 743–753.

Meng, W.; Khayat, K.H. (2018) Effect of graphite nanoplatelets and carbon nanofibers on rheology, hydration, shrinkage, mechanical properties, and microstructure of UHPC. Cem. Con. Res. 105, 64–71.

Meng, W.; Khayat, K. (2017). Effects of saturated lightweight sand content on key characteristics of ultra-high-performance concrete. Cem. Con. Res. 101, 46–54.

Meng, W.; Samaranayake, V.A.; Khayat, K.H. (2018). Factorial design and optimization of ultra-high-performance concrete with lightweight sand. ACI Mater. J. 115, 129–138.

Moroşan, P.D.; Bourdais, R.; Dumur, D. (2010) Buisson, J. Building temperature regulation using a distributed model predictive control. Energy Build. 42, 1445–1452.

Pour-Ghaz, M.; Castro, J.; Kladivko, E.J.; Weiss, J. (2012). Characterizing lightweight aggregate desorption at high relative humidities using a pressure plate apparatus. J. Mater. Civil Eng. 24, 961–969,

Ramesh, S., Choe, L.Y., Seif, M.S., Hoehler, M.S., Grosshandler, W.L., Sauca, A., Bundy, M.F., Luecke, W.E., Bao, Y., Klegseth, M., Chen, G., Reilly, J., Glisic, B. (2019). Compartment Fire Experiments on Long-Span Composite-Beams with Simple Shear Connections Part 1: Experiment Design and Beam Behavior at Ambient Temperature. NIST Technical Note 2054, Gaithersburg, MD.

Rinaudo, P., Torres, B., Paya-Zaforteza, I., Calderón, P.A., Sales, S. (2015). “Evaluation of new regenerated fiber Bragg grating high-temperature sensors in an ISO 834 fire test.” Fire Safety J., 71, 332–339.

Steel Deck Institute. (C-2011). Standard for Composite Steel Floor Deck-Slabs, American National Standards Institute.

Yang, J.C., Bundy, M.F., Gross, J.L., Hamins, A.P., Sadek, F.H., Raghunathan, A. (2015) International R and D Roadmap for Fire Resistance of Structures Summary of NIST/CIB Workshop (NIST SP 1188).

Zhang, B., Kahrizi, M. (2007) “High-temperature resistance fiber Bragg grating.” Sensors, 7, 586–591.